Resource

Cell

B Cells and T Follicular Helper Cells Mediate Response to Checkpoint Inhibitors in High Mutation Burden Mouse Models of Breast Cancer

Graphical Abstract

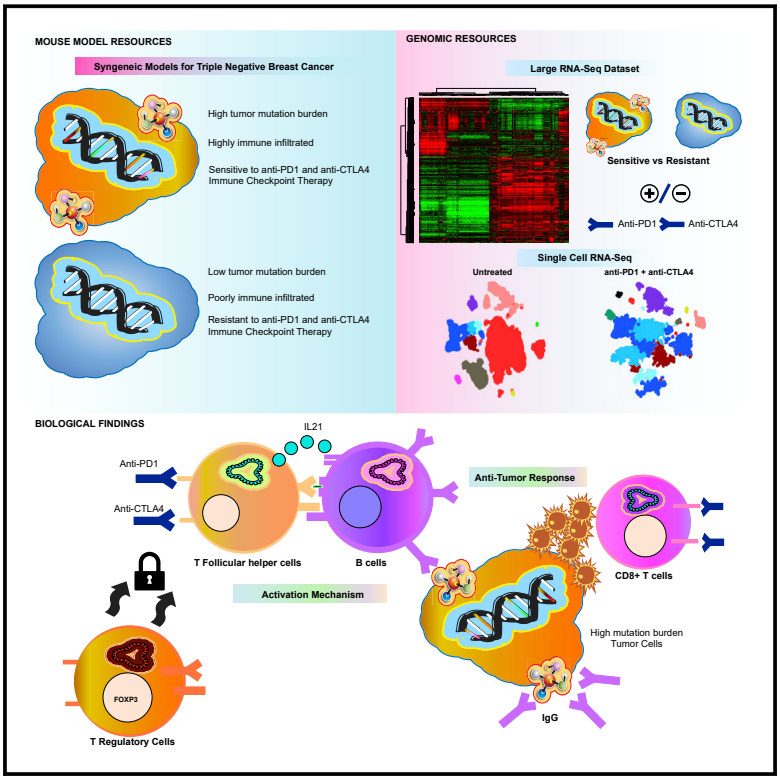

Highlights

- New TNBC murine models with high mutation burden and immune cell activity
- A genomics resource of immune checkpoint treated tumors from TNBC murine models
- Immune checkpoint blockade activates Tfh and B cells in the anti-tumor response
- B cells impact immunotherapy response by secreting antibody and activating T cells

Authors

Daniel P. Hollern, Nuo Xu, Aatish Thennavan, ..., Benjamin G. Vincent, Jonathan S. Serody, Charles M. Perou

Correspondence

cperou@med.unc.edu

In Brief

Mouse models of triple-negative breast cancer provide insights into how T follicular helper cell activation of B cells facilitates the effects of immune checkpoint inhibitors.

Hollern et al., 2019, Cell *179*, 1191–1206
November 14, 2019
https://doi.org/10.1016/j.cell.2019.10.028

CellPress

Cell

B Cells and T Follicular Helper Cells Mediate Response to Checkpoint Inhibitors in High Mutation Burden Mouse Models of Breast Cancer

Daniel P. Hollern,[1,2] Nuo Xu,[3] Aatish Thennavan,[1,2,6] Cherise Glodowski,[1,7] Susana Garcia-Recio,[1,2] Kevin R. Mott,[1,2] Xiaping He,[1,2] Joseph P. Garay,[1,2] Kelly Carey-Ewend,[1,2] David Marron,[1,2] John Ford,[1,2] Siyao Liu,[1,2] Sarah C. Vick,[3] Miguel Martin,[8] Joel S. Parker,[1,2] Benjamin G. Vincent,[1,3,4,5] Jonathan S. Serody,[1,3,4] and Charles M. Perou[1,2,9,*]

[1]Lineberger Comprehensive Cancer Center, University of North Carolina, Chapel Hill, NC 27599, USA
[2]Department of Genetics, University of North Carolina, Chapel Hill, NC 27599, USA
[3]Department of Microbiology and Immunology, University of North Carolina, Chapel Hill, NC 27599, USA
[4]Department of Hematology/Oncology, Department of Medicine, University of North Carolina, Chapel Hill, NC 27599, USA
[5]Curriculum in Bioinformatics and Computational Biology, University of North Carolina, Chapel Hill, NC 27599, USA
[6]Oral and Craniofacial Biomedicine Program, School of Dentistry, University of North Carolina, Chapel Hill, NC, USA
[7]Department of Pathology and Laboratory Medicine, University of North Carolina, Chapel Hill, NC 27599, USA
[8]Instituto de Investigación Sanitaria Gregorio Marañon, CIBERONC, Universidad Complutense, Madrid, Spain
[9]Lead Contact
*Correspondence: cperou@med.unc.edu
https://doi.org/10.1016/j.cell.2019.10.028

SUMMARY

This study identifies mechanisms mediating responses to immune checkpoint inhibitors using mouse models of triple-negative breast cancer. By creating new mammary tumor models, we find that tumor mutation burden and specific immune cells are associated with response. Further, we developed a rich resource of single-cell RNA-seq and bulk mRNA-seq data of immunotherapy-treated and non-treated tumors from sensitive and resistant murine models. Using this, we uncover that immune checkpoint therapy induces T follicular helper cell activation of B cells to facilitate the anti-tumor response in these models. We also show that B cell activation of T cells and the generation of antibody are key to immunotherapy response and propose a new biomarker for immune checkpoint therapy. In total, this work presents resources of new preclinical models of breast cancer with large mRNA-seq and single-cell RNA-seq datasets annotated for sensitivity to therapy and uncovers new components of response to immune checkpoint inhibitors.

INTRODUCTION

Immune checkpoint inhibitors (ICIs) have improved patient outcomes in human cancers (Le et al., 2015; Sharma and Allison, 2015). In many solid tumors, tumor mutation burden (TMB) and, as a result of high TMB, neoantigen load are biomarkers for therapeutic benefit. For example, in colorectal cancers, mismatch-repair status predicted clinical benefit for the anti-PD1 antibody pembrolizumab (Le et al., 2015). In non-small cell lung cancer, a mutation signature linked to smoking predicted anti-PD1 efficacy (Rizvi et al., 2015). In melanoma, TMB and neoantigen load predict patient response to anti-CTLA-4 therapy (Van Allen et al., 2015). The presence of $CD8^+$ T cells(Tumeh et al., 2014) and expression of immune checkpoint genes, such as the PD1 ligand (PD-L1) (Topalian et al., 2012) and CTLA-4 (Herbst et al., 2014), also predict ICI efficacy. These data indicate that predicting response to ICI is multi-factorial and requires additional studies.

In triple-negative breast cancer (TNBC), immune cells identified by pathology (i.e., tumor-infiltrating lymphocytes [TILs]) or by genomic signatures indicate a favorable prognosis (Iglesia et al., 2014; Miller et al., 2016), and chemotherapy efficacy is more likely in tumors with immune infiltrates (Nolan et al., 2017; Tsavaris et al., 2002). In addition to immune infiltration, TNBC tends to harbor higher TMB among breast cancers. Recently, atezolizumab (an anti-PDL1 antibody) plus nab-paclitaxel was shown to prolong progression-free survival in TNBC patients with PD-L1 positive tumors (Schmid et al., 2018). With this success and FDA approval, ICI response rates still range from 10% to 20% (Wein et al., 2018) and atezolizumab's impact on TNBC overall survival is modest. Given lessons from other cancer types, we hypothesized that TMB and immune cell infiltration could be important factors in response to ICIs for TNBC.

In breast cancer, APOBEC3B enzyme activity is linked to mutagenesis of tumor genomes (Burns et al., 2013). APOBEC3B is a cytidine deaminase and, upon activity, creates abasic sites that lead to mutations (Morganella et al., 2016) and potentially neoantigens. Since mutation load predicts ICI response in other cancers (Rizvi et al., 2015; Van Allen et al., 2015) and APOBEC3B activity corresponds with higher TMB in breast cancer (Burns et al., 2013), we created two separate, genetically engineered mouse models (GEMMs) of mammary cancers with overexpression of murine APOBEC3. Similarly, we used short-wave ultraviolet (UV) radiation to create additional high TMB GEMMs. We refer to the lines with intentionally increased TMB as

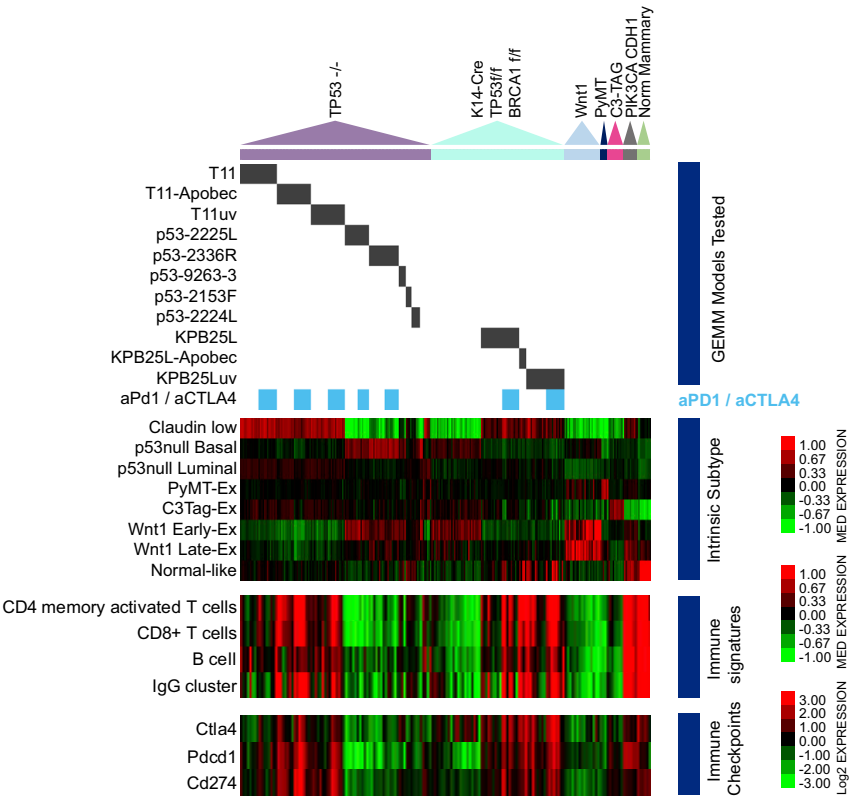

Figure 1. Intrinsic Tumor and Immune Cell Gene Expression Features in Mouse Mammary Tumor Models

Gene expression patterns of tumor and immune cell features. The triangles mark the position of major tumor models in the heatmaps. Black bars mark tumor lines from each model. Blue bars to the side note models in the treatment study. Below this, blue bars show samples getting aPD1/aCTLA4 therapy. The heatmaps show median expression values for subtype and immune cell signatures. The lower heatmap shows expression values of immune checkpoint mRNAs as indicated by the color bar.

"mutagenized lines" and the non-mutated version of each line as its "parental line." Using these and other mouse models of TNBC in a pre-clinical trial of anti-PD1 and anti-CTLA-4 therapy, we identify factors that mediate responses to ICIs, including an important role for $CD4^+$ T follicular helper (Tfh) cells, B cells, and the generation of antibody by those B cells in the anti-tumor response to dual ICIs.

RESULTS

Mouse Models and Genomic Signatures of Immune Cells

To study the response to ICIs and identify predictive biomarkers, we turned to a genetically controlled model system, namely a rich resource of credentialed mouse models of TNBC (Hollern et al., 2019; Pfefferle et al., 2016, 2013). Figure 1 shows the key mRNA features for 290 specimens from multiple GEMMs. Within Tp53−/− and K14-Cre;Tp53f/f; Brca1f/f models, we selected transplantable sublines to establish a cohort for anti-PD1 and anti-CTLA-4 combination therapy

Table 1. Response to Combination Immunotherapy

Model	Genetics	Subtype	Mutation load	Median survival untreated	Median survival aPD1/aCTLA4	10-day response untreated	10-day response aPD1/aCTLA4
2225L	TP53−/−	Basal-like	11	10 days, n = 15	9.5 days, n = 18	3,951 ± 172, n = 15	3,098 ± 315, n = 18
2336R	TP53−/−	Basal-like	50	19 days, n = 22	18 days, n = 25	1,319 ± 324, n = 22	1,372 ± 313, n = 25
2224L	TP53−/−	Basal-like	39	9 days, n = 22	9 days, n = 22	3,108 ± 219, n = 22	2,905 ± 224, n = 22
9263-3F	TP53−/−	Basal-like	87	9 days, n = 8	9 days, n = 7	3,868 ± 255, n = 8	4,123 ± 0, n = 7
2153F	TP53−/−	Luminal-like	57	12.5 days, n = 18	11 days, n = 17	2,906 ± 312, n = 18	3,183 ± 282, n = 17
T11	TP53−/−	Claudin-low	117	13 days, n = 20	12 days, n = 16	2,149 ± 265, n = 20	2,721 ± 324, n = 16
T11-Apobec	TP53−/−; Apobec3 overexpressed	Claudin-low	374	14 days, n = 19	38 days, n = 40*	1,782 ± 307, n = 19	76 ± 37, n = 40*
T11-UV	TP53−/−; Short-wave UV exposure	Claudin-low	1,783	11 days, n = 12	25 days, n = 16*	2,547 ± 356, n = 12	452 ± 107, n = 16*
KPB25L	K14-Cre; TP53 f/f Brca1 f/f	Basal-like	181	21 days, n = 17	28 days, n = 13*	1,670 ± 383, n = 17	260 ± 869, n = 13*
KPB25L-Apobec	K14-Cre; TP53 f/f Brca1 f/f; Apobec3 overexpressed	Basal-like	309	43 days, n = 11	64 days, n = 13*	125 ± 30, n = 11	−12 ± 16, n = 13*
KPB25L-UV	K14-Cre; TP53 f/f Brca1 f/f; Short-wave UV exposure	Basal-like	316	37 days, n = 26	74 days, n = 26*	230 ± 60, n = 26	−22 ± 7, n = 26*

* denotes $p < 0.05$ in comparison to untreated cohort; 10 day response = change in volume m3m, ± SEM.

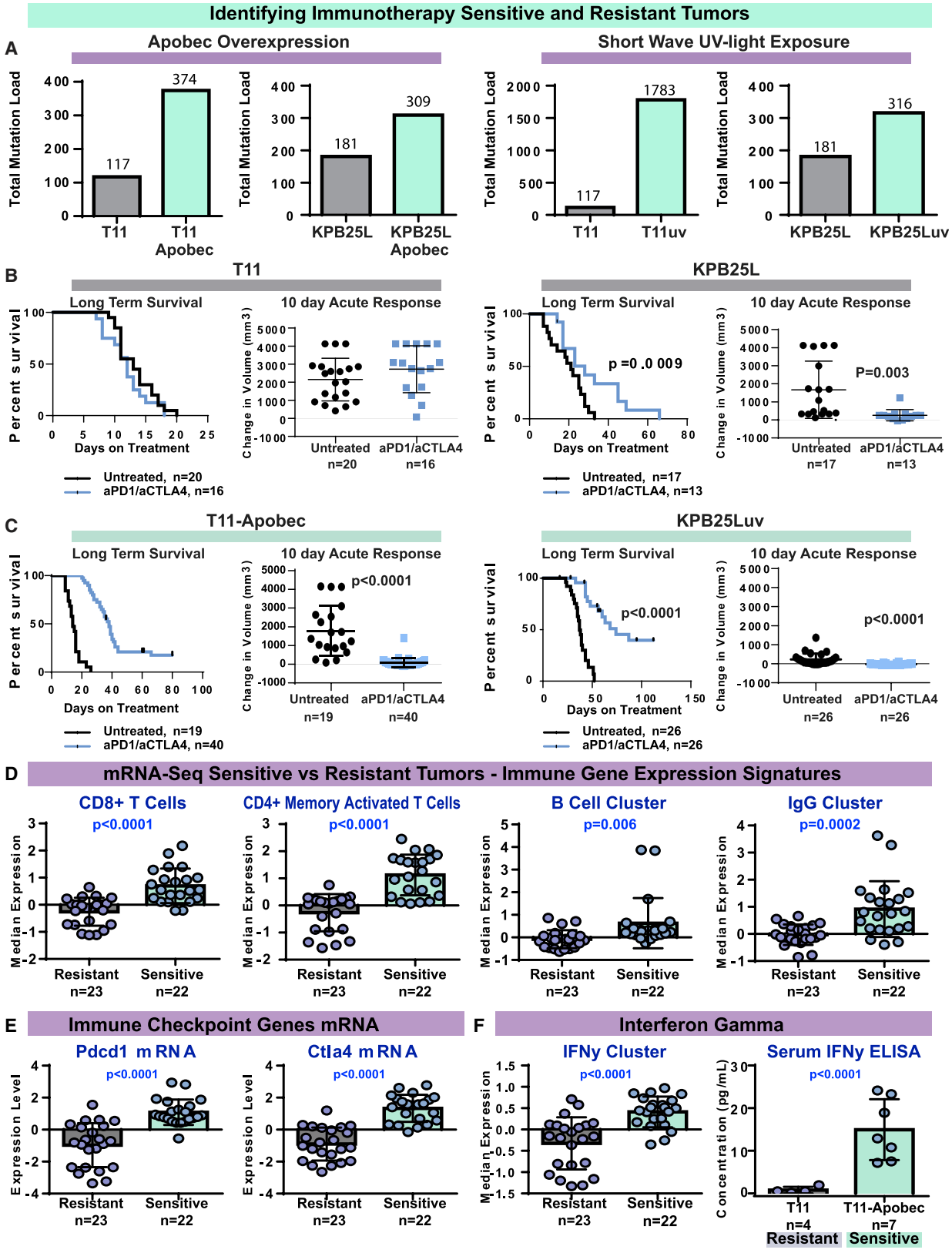

(legend on next page)

(abbreviated as aPD1/aCTLA4 or ICI; 7 models used for initial ICI testing). Our work here focused on experimentation, predominately in two different GEMMs: Tp53−/− tumor syngeneic transplant derived cell line (T11) and a cell line from a K14-Cre;Tp53f/f; Brca1f/f tumor (KPB25L). Other treated GEMMs are listed in Table 1. These mouse models of TNBC represent multiple subtypes (i.e., basal-like and claudin-low [Parker et al., 2009; Pfefferle et al., 2013]) and show expression of signatures for $CD4^+$ T cells, $CD8^+$ T cells, B cells, and immunoglobulin G (IgG) (Figure 1). Diverse expression of immune checkpoint genes Pdcd1, Cd274 (Pd-l1), and Ctla4 was also noted in the seven syngeneic, transplantable murine lines used for testing ICI therapy.

Testing GEMMs of Mammary Cancer with ICIs

Initial testing with aPD1/aCTLA4 therapy in TNBC GEMMs showed no response in six out of seven tumor lines (Table 1; Figure S1A). Resistant GEMMs had a low TMB (Figure S1B) and a low predicted neoantigen burden (Figure S1C). Murine tumors had lower TMBs than typically found in human breast cancer, considerably lower than ICI-responsive human non-small-cell lung carcinomas (NSCLCs) and melanomas (Figure S1D). The lone (moderately) sensitive model was a BRCA1-deficient tumor line (KPB25L), which had higher relative TMB. Thus, we posited that, to accurately reflect the ICI response clinically, we needed to develop additional models that reflect the higher TMB of human cancers. Because Apobec3 is linked to mutagenesis of breast cancer (Burns et al., 2013) and immune cell infiltrates (Budczies et al., 2018; Smid et al., 2016; Wang et al., 2018), we hypothesized that Apobec3 could elevate the mutation load and number of predicted neoantigens, possibly sensitizing a previously resistant GEMM tumor to ICI therapy. Similarly, we hypothesized exposure to UV radiation could lock in new mutations to create high-TMB models and improve ICI sensitivity. Indeed, Apobec3 overexpression (T11-Apobec, KPB25L-Apobec; Figure 2A) and UV exposure (T11-UV, KPB25Luv; Figure 2B) markedly increased TMB as compared with the matched time-in-culture parental cell lines (T11, KPB25L). As expected, having a higher TMB also led to a higher predicted neoantigen load in major histocompatibility complex (MHC) haplotype-compatible lines (Figure S1C).

In support of the TMB and neoantigen hypothesis of ICI responsiveness, the parental lines showed little sensitivity to aPD1/aCTLA4 therapy (Figure 2B) while the mutagenized lines had robust responses (Figures 2C and S1E). The response data for all sensitive and resistant lines are shown in Figure S1 and Table 1. Table S1 lists hazard ratios for every survival endpoint in this report. We also tested single-agent aPD1 and aCTLA4 and noted that, while sometimes effective, single ICIs were inferior to combinations (Figure S1F). Testing isotype controls confirmed that response to therapy was not driven by the presence of exogenous IgG2a or IgG2b antibodies (Figure S1G), consistent with the lack of any therapeutic effect in resistant lines. As controls, Apobec3 overexpression and UV-based mutagenesis strategies did not impact proliferation *in vitro* (Figure S2). All together, these results signify TMB as a key marker for ICI efficacy in the murine TNBC models tested here.

Genomic Analysis of ICI-Treated GEMM Tumors

To test for additional predictors of response to ICI therapy, we examined pretreatment tumors (5 mm in diameter) from sensitive and resistant models with mRNA sequencing (mRNA-seq). Published mRNA signatures for $CD4^+$ T cells (Newman et al., 2015), $CD8^+$ T cells (Fan et al., 2011), B cells (Iglesia et al., 2014), and IgG (Fan et al., 2011) each correlated with response (Figure 2D). Levels of immune checkpoint genes Pdcd1 and Ctla4 (Figure 2E) as well as interferon-gamma (serum and tumor; Figure 3C) were also significantly higher in sensitive tumors. Thus, we hypothesized that our mRNA-seq data may enable the development of new mRNA-based biomarkers. We therefore performed supervised analyses to derive signatures differentiating sensitive from resistant tumors. Given that functionally related genes often covary, we used hierarchical clustering and SigClust (Huang et al., 2015) to identify metagenes of statistical significance and probable biological meaning (Figure 3A; Data S1). This identified a large cluster of immune cell genes (immune activity cluster) and a smaller node of B cell genes, IgGs, and T cell genes (Figure S3A) that is henceforth referred to as the B cell/T cell co-cluster.

Human Patient Studies

To test the clinical value of these two new genomic signatures, we used published data from multiple human clinical studies. This included two melanoma datasets of patients treated with ICIs (Sade-Feldman et al., 2018; Van Allen et al., 2015), three human breast cancer datasets from clinical trials of neoadjuvant chemotherapy (Echavarria et al., 2018; Esserman et al., 2012; Miyake et al., 2012), and one human breast cancer dataset that is a clinical trial of neoadjuvant trastuzumab + paclitaxel (Tanioka et al., 2018). In each dataset, the B cell/T cell co-cluster was significantly higher in pretreatment samples from patients who responded to therapy (Figures 3B–3G). Similar results were noted for the immune activity cluster (Figures S3B–S3G); however, one exception was seen in the human melanoma

Figure 2. Intentional Elevation of Tumor Mutation Burden Sensitizes Tumors to aPD1/aCTLA4 Combination Therapy

(A) Left: total somatic mutation burden in ectopic Apobec3 overexpressing lines and parental control lines. Right: somatic mutation burden from parental lines and lines exposed to short-wave ultraviolet radiation.

(B) Survival and 10-day acute response to aPD1/aCTLA4 immune checkpoint therapy in mice bearing tumors from parental T11 cell line and KPB25L cell lines.

(C) Survival and acute response in T11-Apobec and KPB25Luv lines.

(D) Immune cell gene expression signature expression levels.

(E) Immune checkpoint gene mRNA expression levels.

(F) Left: interferon-gamma signature expression levels. Right: serum interferon-gamma as measured by ELISA. In boxplots, bars mark the average and standard deviation. The p values are two-tailed from unmatched t tests. In Kaplan-Meier plots, p values are from Log-rank (Mantel-Cox) tests. Signature levels are calculated as median value of genes within, and mRNA is the median centered Log2 expression level.

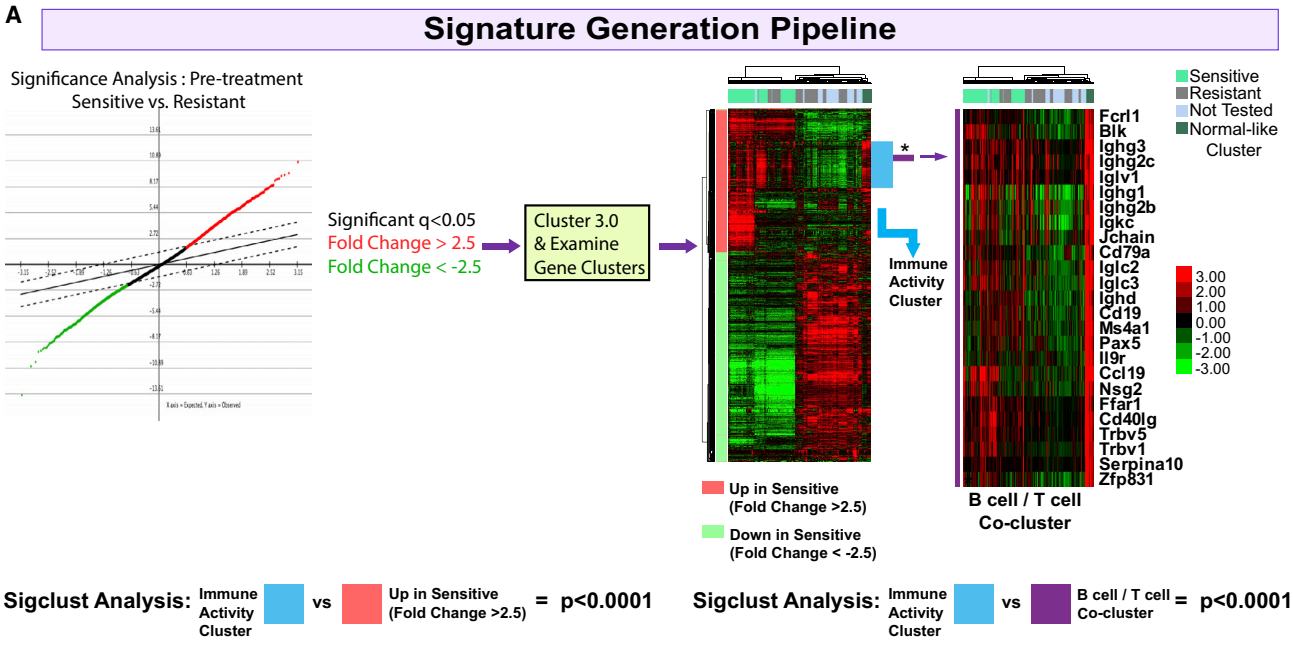

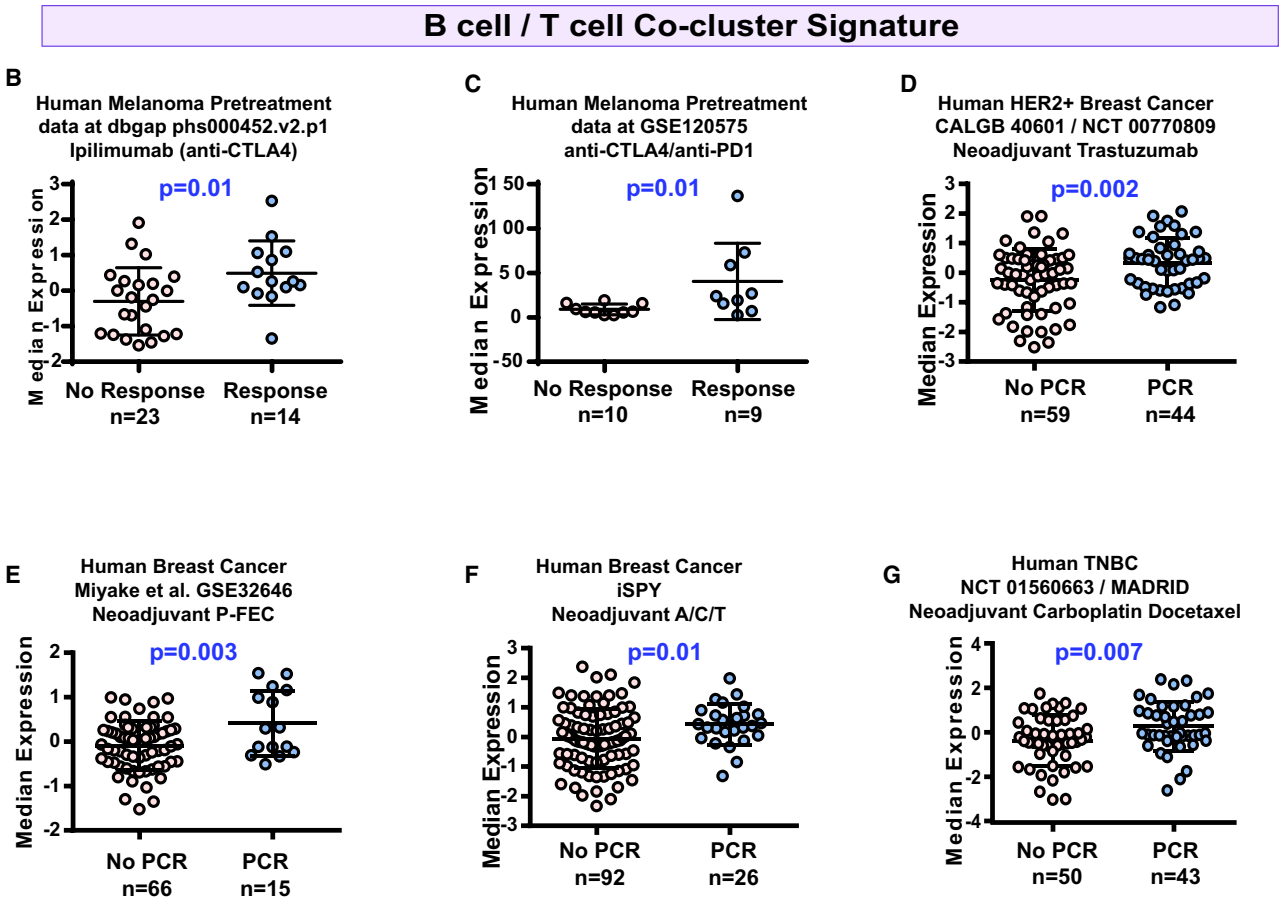

Figure 3. Signature Testing on Human Studies

(A) Signature development pipeline. The immune activity signature is noted by the blue bar near the heatmap. The B cell/T cell co-cluster is marked by the purple bar and featured.

(legend continued on next page)

dataset that used single-cell profiling of CD45$^+$ cells, where the immune activity cluster was not predictive but the B cell/T cell co-cluster was. Given that equal numbers of CD45$^+$ cells were profiled in responder and non-responder groups, similar expression of the generic immune activity cluster was expected. Thus, when examining even numbers of total immune cells, higher representation of B cell populations seems to predict response in human breast and melanoma tumors.

Immune Cell Response to Therapy

To test whether these immune cell features are also activated by ICI therapy, we examined tumors after 7 days with or without ICI therapy using mRNA-seq. No significant changes were seen in immune signatures for resistant tumors. In sensitive lines treated with ICIs, mRNA-seq again identified significant elevation in CD4$^+$ T cells, CD8$^+$ T cells, B cells, and IgG signatures (Figure 4A). Flow cytometry analysis (for gating, see Figure S4) confirmed T cell signatures and revealed expanded CD8$^+$ and CD4$^+$ effector memory T cells with therapy in sensitive models (Figure 4B). Flow cytometry also verified B cell signatures, with aPD1/aCTLA4-treated tumors presenting a striking increase in activated B cells (Figures 4C and 4D). Strong concordance between mRNA-seq and flow cytometry was also seen within each tumor model (Figures S5A–S5C). The IgG signature predicted the potential for B cell class switching and antibody responses. To confirm this prediction, we first used immunohistochemistry (IHC). Indeed, IHC showed that ICIs increased the number of IgG-positive cells within the tumor (Figure 4E). To test secretory antibody activity, we examined serum IgG binding to cells kept *in vitro*. Here, we noted a significant increase in IgG binding against KPB25Luv cells in ICI-treated mice (Figure 4F), with specificity marked by low off-target binding (Figure 4G). Additional tests implied a possible IgG target(s) specific to the mutagenized line as well as a shared target(s) with the parent line (Figure S5D). Treatment also increased serum IgG specific to tumor cells in the T11-Apobec model (Figure 4H). Finally, ICIs did not substantially increase T cells in T11 parental tumors (Figure S5E). High CD8 to T regulatory cell (T_{reg}) ratios were exclusive to mutagenized tumors (Figure S5F), suggesting that mutations and neoantigens are key to the release of immune suppression and a shift toward a productive anti-tumor response featuring activated T cells and B cells.

Single-Cell RNA-Seq

To precisely define the responding T cell and B cell subsets, we examined KPB25Luv (Figure 5) and T11-Apobec (Figure S6) tumors after 7 days with or without ICIs using single-cell RNA-seq (scRNA-seq). Untreated tumors had an abundance of tumor cells, neutrophils, and macrophages, with a variety of other cell types presenting at lower frequencies (Figures 5A and S6A). With aPD1/aCTLA4 therapy, prominent changes in the distribution of cell types identified were noted. In particular, tumor cells, neutrophils, and macrophages were reduced, while T cells and B cells were expanded (Figures 5A, 5B, S6A, and S6B). In addition, a plasma cell cluster was identified, unique to treated tumors. Changes in these cell types were also reflected in supervised analyses comparing tumors with and without therapy (Figures 5C and S6C).

In both GEMMs tested, effector memory CD8$^+$ T cells were expanded by therapy. Accordingly, scRNA-seq showed a significantly higher abundance of cells with Cd8a expression (Figures 5D and S6D). Significance testing of ICI-treated CD8$^+$ clusters revealed that proliferation and cytotoxic genes increased in CD8$^+$ T cell subsets (Figures 5E and S6E). Among cells with cytotoxic gene expression profiles, cells with high expression of checkpoint and exhaustion markers Eomes, Pdcd1, Ctla4, Lag3, and Tim3 were frequent (Figures 5G and S6G) (Wherry and Kurachi, 2015). We also noted CD8$^+$ subsets that were unique to KPB25Luv tumors, with one having high expression of Eomes and another with high Ccr10 mRNA (Figures 5E–5G). The Ccr10-high CD8$^+$ T cells were also marked by expression of Cxcr3 and genes involved in cell migration, which is indicative of T cells trafficking to sites of inflammation (Eksteen et al., 2006; Qin et al., 1998). High EOMES and PD1 with low T-BET (TBX21) are known to mark terminal exhaustion and minimal capacity to respond to ICIs (Pauken et al., 2016). Yet, the Eomes-high CD8$^+$ T cell cluster in KPB25Luv tumors lacked high Pdcd1 expression and had moderate Tbx21 levels. Together, these data show the CD8$^+$ T cells to contain proliferating and cytotoxic effector memory cells.

Cells expressing Cd4 mRNA were significantly increased with ICI therapy (Figures 5H and S6H). When examining treated sensitive tumors, differentially expressed genes among CD4$^+$ clusters identified T cells with high expression of proliferation genes (Figures 5I and S6I). This analysis also identified a large group of T_{regs} mixed with naive-like subsets in T11-Apobec. In contrast, T_{regs} were distinct from other CD4$^+$ subsets (Figure 5A) in the KPB25Luv model. Marker analysis also identified significant genes for a cluster of CD4$^+$ cells resembling Tfh cells (Figures 5I and S6I). This included well-known markers such as Cxcr5, Cd154 (Cd40l), Pdcd1, Maf, and Il21 (King, 2009). These Tfh-associated genes showed a clear distinction between the naive- and Tfh-like clusters in KPB25Luv (Figures 5I–5K). Similar results were found in T11-Apobec, adding that Tfh-like cells were also present in the proliferating group. With Pdcd1, many of the Tfh-like cells also had high expression of Ctla4. Collectively,

(B) Boxplot for the B cell/T cell co-cluster in pretreatment samples from a human melanoma study of aCTLA4 therapy (Van Allen et al., 2015).
(C) Boxplot of the B cell/T cell co-cluster in pretreatment samples from a human melanoma study of aPD1/aCTLA4 therapy (Sade-Feldman et al., 2018).
(D) Boxplot of the B cell/T cell co-cluster in pretreatment breast cancer samples from CALGB40601, trastuzumab arm (Tanioka et al., 2018).
(E) Boxplot of the B cell/T cell co-cluster in pretreatment samples from the human breast cancer dataset GSE32646, P-FEC, neoadjuvant paclitaxel followed by 5-fluorouracil, epirubicin, and cyclophosphamide therapy (Miyake et al., 2012).
(F) Boxplot of the B cell/T cell co-cluster in pretreatment samples from the human breast cancer iSPY clinical trial; A/C/T arm = Doxorubicin hydrochloride and cyclophosphamide, followed by treatment with paclitaxel (Esserman et al., 2012).
(G) Boxplot of the B cell/T cell co-cluster in pretreatment samples from the TNBC NCT 01560663 clinical trial (Echavarria et al., 2018). Boxplots mark the mean and standard deviation. All panels except (C), the p values show two-tailed p value from standard t tests; in (C), data are non-Gaussian, and thus a Mann-Whitney test was used.

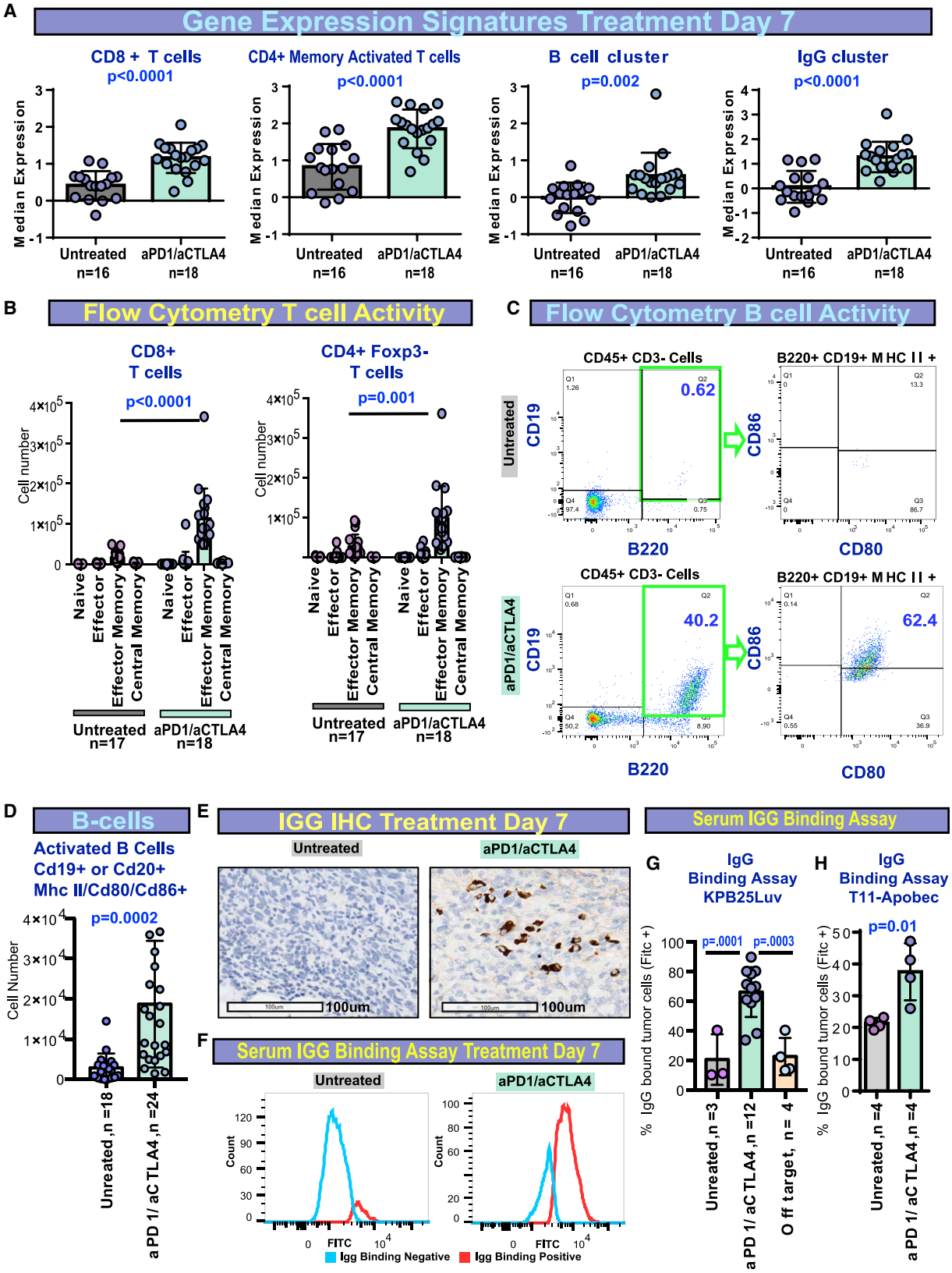

(legend on next page)

these data depict the dominant effector memory subset of CD4+ T cells to be Tfh cells.

Markers for B cells were also associated with ICI therapy in scRNA-seq (Figures 5L and S6L) and depicted various stages of B cell activation in treated sensitive tumors (Figures 5 and S6M–O). For example, in KPB25Luv tumors, B cells were separated on the B cell receptor (BCR) isotype. Non-class-switched B cells had high expression of MHC class II genes and other activation markers. Class-switched B cells were marked by high expression of proliferation genes, Aicda, and Ighg1 (and low Ighd); thus, these B cells resemble those class-switched B cells undergoing somatic hypermutation. While this cluster was not detected in T11-Apobec, probing for these genes identified these cell types among the B cells present in this tumor model. Both models showed a distinct cluster of cells with gene expression profiles matching that of plasma cells. These cells were marked by high expression of IgG (Ighg1, Ighg3), which indicates class switching and the dominant antibody types induced by ICIs.

TCR and BCR Clonality

To understand the selectivity of the T cell and B cell response, we used 5′ RACE-like sequencing to measure BCR and T cell receptor (TCR) clonality in ICI-treated KPB25Luv (Figure 5P) and T11-Apobec (Figure S6P) tumors. Perhaps related to differences noted by scRNA-seq, T cells in T11-Apobec were more clonally restricted than KPB25Luv. In fact, the top three clones in T11-Apobec (Shannon entropy = 4.22) accounted for 40% of TCR-alpha expression compared with 14% in KPB25Luv (Shannon entropy = 5.58) tumors; TCR-beta sequences matched these trends. Assessing BCR diversity, both models were clonal. The top clone of the heavy chain (BCR-H) alone made up 41% of sequences in KPB25Luv (Shannon entropy = 2.05) and 54% of sequences in T11-Apobec (Shannon entropy = 2.18). Light-chain mRNA also showed a high degree of clonal restriction (BCR-lambda) (Shannon entropy KPB25Luv = 0.68; T11-Apobec = 1.75). Collectively, these data show significant evidence of immune-adaptive-cell clonal selection.

Role of B Cells and T Cells in Response to ICIs in Murine Models

The B cell/T Cell co-cluster signature predicted ICI response in human cancers, and both B cells and T cells showed robust expansion following therapy. Thus, it was critical to test whether these cell types were essential to ICI efficacy in our *in vivo* models. Hence, we individually depleted CD4+ T cells, CD8+ T cells, or B cells using antibodies (Figure S7) during aPD1/aCTLA4 therapy. In each case, depletion of these populations (i.e., CD4+, CD8+, CD19+, CD20+) significantly reduced the therapeutic response to aPD1/aCTLA4 therapy as assessed by survival (Figures 6A and 6C) and short-term response (i.e., tumor volume changes) (Figures 6B and 6D). The most prominent effects were observed in the CD4+ T cell-depleted mice and B cell-inhibited and/or B cell-depleted mice (CD19 or CD20, respectively), where therapeutic benefit was completely ablated.

B cells are known to present antigens to T cells (Hong et al., 2018; Nelson, 2010), prompting us to test the impact of B cell activity on T cells. Interestingly, both CD8+ and CD4+ T cells were reduced by B cell inhibition (Figure 6E). In CD8+ subsets, the effector and effector memory T cells were reduced. In the CD4+ T cells, effector memory and central memory subsets were diminished by B cell inhibition. Together, these data indicate the generation of T cell memory is in part dependent on the function of B cells.

Our B cell/T cell co-cluster also suggested that B cell activity may be similarly dependent on T cells. Indeed, CD4+ T cells are known regulators of B cell activity(Clark and Ledbetter, 1994). To formally test this, we first tested whether CD4+ T cell depletion impacted B cell infiltration and activation during ICI therapy by flow cytometry. ICI-treated tumors depleted for CD4+ T cells resembled non-treated tumors (Figure 7A), showing minimal B cell infiltration in the tumor (Figure 7B). As such, we sought to identify which CD4+ subset was involved in the mechanism of B cell activation. To predict the CD4+ cell type responsible for activating B cells, we used the bulk mRNA-seq and scRNA-seq data. Published signatures for Th1 (Figure S8A) and Th2 (Figure S8B) subsets did not correlate with B cell signatures nor show elevation with therapy in mRNA-seq data in sensitive models. Similarly, Th1, Th2, and Th17 cytokines were rarely expressed the scRNA-seq transcriptome data, suggesting that these cells are not commonly found in ICI-treated tumors (Figures S8C and S8D). However, published signatures for Tfh cells strongly correlated ($p < 0.0001$) with B cell signatures in mRNA-seq of ICI sensitive tumors (day 7) (Figure 7C) and were significantly elevated upon aPD1/aCTLA4 therapy (Figure 7D). Similar results were found for the Tfh cytokine IL-21 (if protein; if gene, Il21) (Figures 7E and 7F). This is consistent with scRNA-seq data (Figures 5 and S6I–6K), showing increased expression of IL21 and a large cluster of cells with Tfh-like expression profiles present with ICI therapy.

To test whether B cell activation by ICI therapy was reliant on Tfh cells, we used antibodies against IL21 to neutralize Tfh activity (Vogelzang et al., 2008). IL21 blockade during aPD1/aCTLA4 therapy significantly reduced B cell activity in both KPB25Luv and T11-Apobec tumors (Figures 7G, S8E, and S8F). Given

Figure 4. Features of Response to aPD1/aCTLA4 Therapy in Murine Tumors

(A) RNA-seq signatures for sensitive tumors at 7 days (5 mm = day 0 or treatment initiation) without or with aPD1/aCTLA4 therapy.

(B) Flow cytometry results for CD8+ cells and CD4+ using memory markers (Cd44, Cd62L).

(C) Flow cytometry of tumor-infiltrating B cells with or without ICI therapy. The right shows staining for B cells gated for activation markers.

(D) Quantification of flow cytometry for activated B cells (B220+, Cd19+ or Cd20+, MHC II+, Cd80+, or Cd86+).

(E) IHC staining for IgG-kappa chain in KPB25Luv tumors.

(F) IgG binding assay showing serum-IgG binding (Fitc+) to KPB25Luv cells.

(G) Quantification of Fitc+ cells in IgG binding assay for KP25Luv cells and off-target binding.

(H) Quantification of Fitc+ IgG binding assay for T11-Apobec cells following reabsorption on off-target cells. In boxplots, bars signify the mean and standard deviation. The p values are two-tailed from unmatched t tests. All tumors collected after 7 days of treatment or non-treatment.

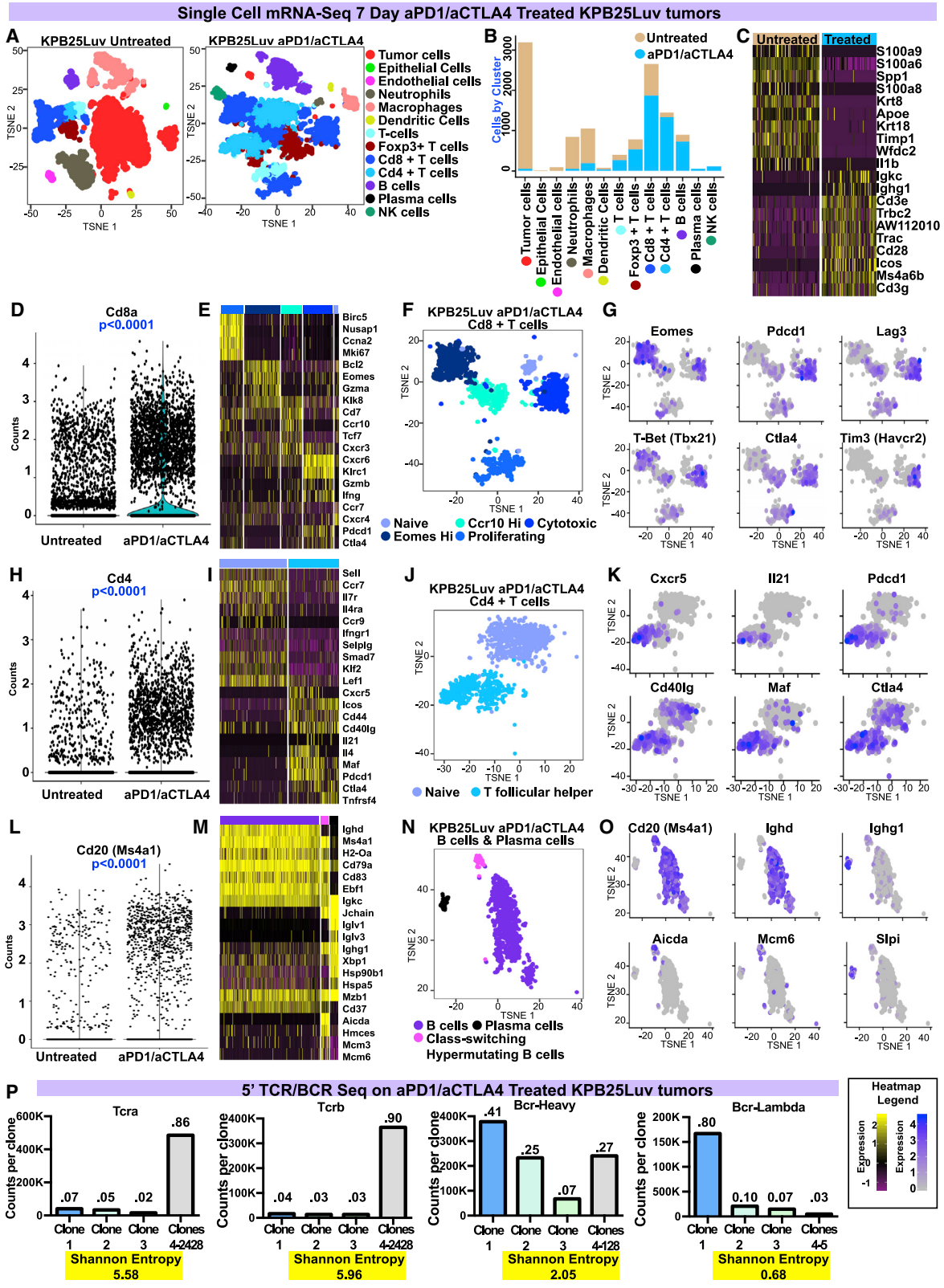

(legend on next page)

that IL21 is known to support class switching and plasma cell generation, we also examined IgG staining by IHC. This revealed that blocking IL21 during ICI therapy sharply reduced the number of IgG$^+$ cells (Figures 7H and S8G). These data indicate a critical role for the activity of Tfh cells in the generation of antibody after dual ICIs. TNBC is often infiltrated with T_{regs}, which may be critical to inhibiting the adaptive immune response. As the function of T_{regs} is somewhat dependent on regulatory CTLA-4 signaling (Peggs et al., 2009), we wondered whether blocking T_{reg} activity may explain the additive effect of combining aPD1 and aCTLA4 on B cell activation (Figures S5A and S5B). Thus, we used a mouse model where FOXP3$^+$ cells (T_{regs}) can be specifically and temporally ablated by diphtheria toxin (Taylor et al., 2017) to test their impact on B cell activation. As suspected, ablation of FOXP3$^+$ cells increased the presence of activated B cells (Figure S8H). Together, these data imply that the optimal B cell activity and therapeutic benefits coming from aPD1/aCTLA4 therapy correlated with concurrent T_{reg} inhibition and Tfh activation. To test the importance of Tfh cell and IL21 activity for ICI benefit, we examined response of mice given aPD1/aCTLA4 therapy with IL21 blockade. This markedly diminished the anti-tumor response (Figures S8I and S8J) and survival in KPB25Luv (Figure 7I) and T11-Apobec (Figure 7J) tumors. As a whole, these data indicate Tfh cells to be critical to ICI efficacy by activating B cells to amplify the anti-tumor immune response.

B cell activation by ICI therapy also led to the generation of class-switched plasma cells (IgHg1, IgHg3) (Figures 5 and S6M–6O), and tumor-specific serum IgG increased following therapy. Moreover, IgG genes were a central part of our highly predictive B cell/T cell signature. This implied that production of IgG against tumor cells was important in mediating response to ICIs. To test this, we utilized a novel mouse model (IgMi) (Waisman et al., 2007) that is immune intact where B cells can be activated but are incapable of antibody secretion (verified in Figures 7K and S8K). Remarkably, the loss of antibody secretion during ICI therapy diminished the initial anti-tumor response (Figure 7L) and survival (Figure 7M) in T11-Apobec bearing mice. As IgMi mice are not available on an FvB background, we used a neutralizing aCD16 monoclonal antibody to evaluate the role of secretory Ig in the KPB25Luv model (Turner et al., 2017) (Figures S8L and S8M). This also led to diminished responses to ICI therapy when assessed by overall survival (Figure 7N). These data for the first time indicate a critical role for antibody secretion in the function of ICI therapy.

DISCUSSION

Identifying predictive biomarkers for human cancer patients is critically important for improvements in immunotherapy and is the foundation of precision medicine. GEMMs of human cancers are often used to investigate the mechanistic impact of specific genetic alterations but, in general, have yielded few clinically relevant biomarkers. The lack of public genomic data on ICI-treated human TNBC limited our human-to-mouse TNBC comparisons. Thus, to seek translational evidence, we tested our possible biomarker for ICI therapy response on multiple clinical datasets covering a number of different therapeutic settings and cancer types.

This study provides a robust genomic dataset—and a novel syngeneic murine tumor resource—for further investigations into the immune microenvironment using a reproducible and genetically controlled animal model system. In particular, we have created a new set of transplantable TNBC mouse model tumors that have high TMB and are sensitive to ICI therapies. It was necessary to develop these new mutagenized models for studying immunotherapy in TNBC, as the majority of GEMM mammary tumor models were resistant and had TMB much lower than typically present in human breast tumors. As stated, these mutagenized GEMMs are uniquely immune activated and therefore will be ideal for future studies of immune cell dynamics and testing novel immunotherapies. In addition, we provide a unique resource of mRNA-seq and scRNA-seq data with fluorescence-activated cell sorting (FACS)-validated changes in immune features.

Our ICI-responsive mutagenized models came from genomically credentialed Tp53−/− (Jerry et al., 2000) and K14-Cre;Tp53f/f; Brca1f/f (Hollern et al., 2019) GEMMs that parallel human TNBC in somatic mutations, copy-number changes, and gene expression profiles (Herschkowitz et al., 2012; Hollern et al., 2019; Pfefferle et al., 2016). While mutation sharing in

Figure 5. Single-Cell RNA-Seq of KPB25Luv Tumors with or without aPD1/aCTLA4 Therapy

(A) t-distributed stochastic neighbor embedding (TSNE) analysis of cells that passed quality checks in KPB25Luv tumors. Cells and clusters are color coded by the major cell type found.

(B) The distribution of cell types between treated and non-treated tumor cells.

(C) Heatmap of mRNA variance between treated and non-treated tumor cells.

(D) Violin plot of Cd8a mRNA levels.

(E) Heatmap of significant genes (plus Pdcd1, Ctla4) in clusters of ICI-treated CD8$^+$ T cells.

(F) Classification of ICI-treated CD8$^+$ T cell clusters. Classes are coded to the heatmap in (E).

(G) Feature plot showing expression of key genes across CD8$^+$ T cell clusters.

(H) Violin plot of Cd4 mRNA levels.

(I) Heatmap of significant genes (plus Ctla4) in clusters of ICI-treated CD4$^+$ T cells (n = 20)

(J) Classification of ICI-treated CD4$^+$ T cell clusters. Classes are coded to the heatmap in (I).

(K) Feature plot showing expression of key genes across CD4$^+$ T cell clusters.

(L) Violin plot of Cd20 mRNA levels.

(M) Heatmap of significant genes in clusters of ICI-treated B cells (n = 20).

(N) Classification of ICI-treated B cell clusters. Classes are coded to the heatmap in (M).

(O) Feature plot showing expression of key markers in B cell clusters.

(P) Results of 5′ TCR and BCR sequencing. In bar plots, read counts for each clone are shown along with the calculated Shannon entropy (where higher values indicate high diversity and low clonality). Above each bar, the percent of all reads occupied by a clone(s). Heatmap values are depicted in the legend. Violin plots mark the mean and SEM. Markers were identified using Seurat and Wilcoxon rank-sum testing.

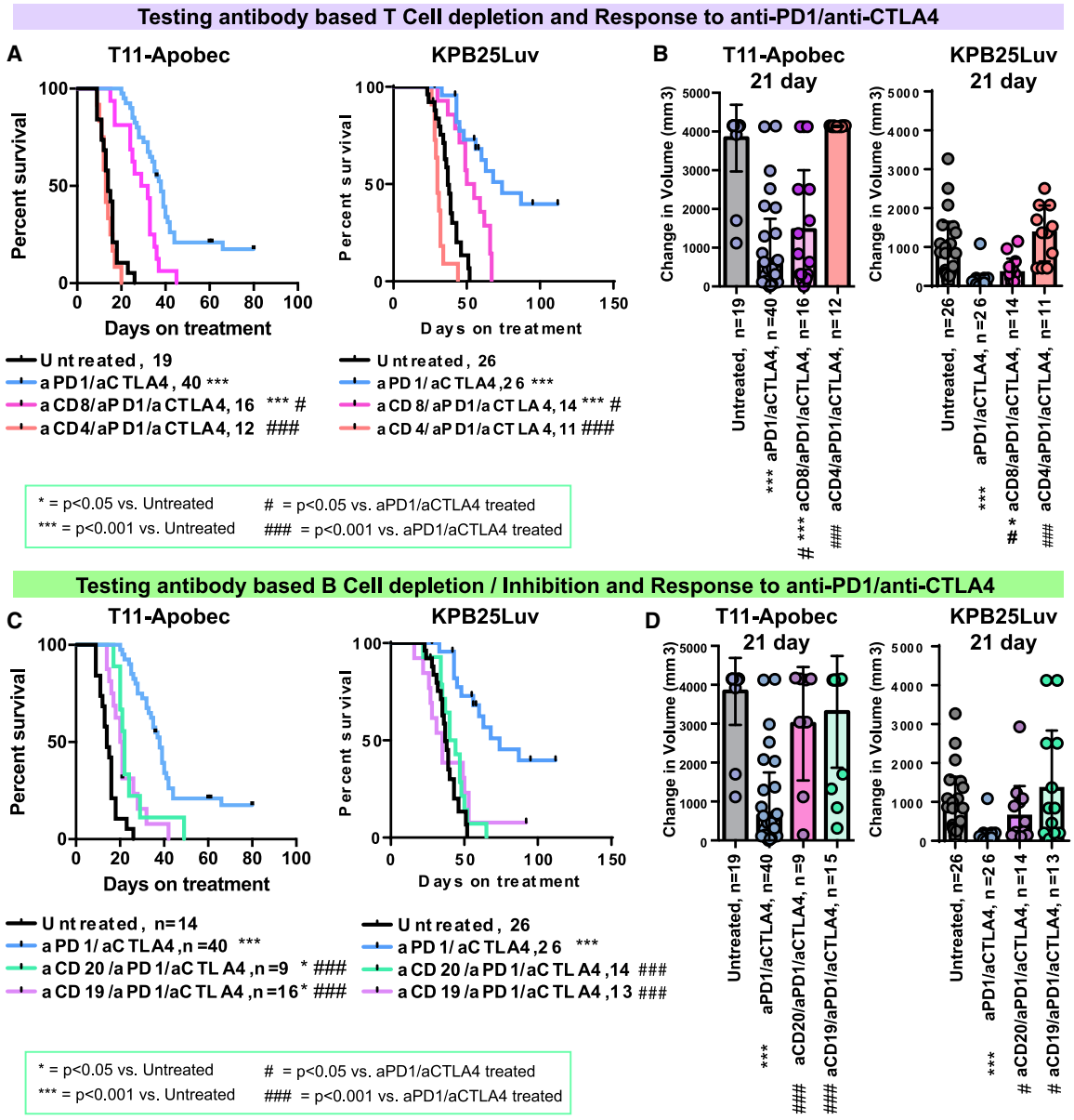

(legend on next page)

TNBCs is low among human breast cancer patients (Network, 2012), save for a few drivers such as TP53 and BRCA1, we did aim to mimic human breast cancer mutagenesis with use of our BRCA1-deficient and APOBEC3 overexpression models. While UV-induced high TMB does not mimic the typical means for breast cancer mutagenesis, it is not evident in the clinical data that the process leading to increased TMB is as critical to ICI response as the presence of high TMB. Indeed, smoking, UV, Apobec, and homologous recombination deficiency mutation signatures were tested across KEYNOTE trial patients and showed no value over TMB alone in the ability to predict ICI benefit (Cristescu et al., 2018). In agreement, the means to obtain high TMB did not relate to response in our GEMMs, namely APOBEC3 or UV-induced high TMB, and this created higher sensitivity in both GEMMs. Yet, more studies are needed to clarify whether mutational process impacts ICI response.

While our two GEMMs had many similarities, we also noted differences between the various mutagenized lines corresponding to the parent model (T11 versus KPB25L), which may be linked to contrasts in their TNBC subtypes (claudin-low versus basal-like). In particular, KPB25Luv and T11-Apobec models differed in their responsiveness to single-agent ICI. In KPB25Luv tumors, individual aPD1 or aCTLA4 were equally effective in activating B cells and the anti-tumor immune response. However, in T11-Apobec, aCTLA4 was clearly more effective in eliciting B cell activation and therapeutic response. Given that CTLA-4 signaling is critical to the function of T_{regs} (Peggs et al., 2009), we believe this to be related to the critical role of T_{regs} in suppressing the immune response, which is intrinsic to T11 tumors via tumor cell CXCL12 secretion (Taylor et al., 2017). This appears to be a general feature found in the claudin-low subtype. Indeed, genetic ablation of T_{regs} in T11-Apobec was sufficient to induce increased B cell activation (Figure S8H). Variances in these models were also noted for $CD8^+$ subsets and T cell clonality. Collectively, these differences in GEMMs add resource value, where individual models can be selected for growth rate, high or low ICI sensitivity, or composition of the microenvironment.

Demonstrating the utility of the resources presented here, we have used these models to identify a new component of response to ICI therapy involving B cells and Tfh cells. Importantly, our findings here are distinct from prior findings detailing PD1 activity in B cells (Thibult et al., 2013; Wang et al., 2019). For example, Thibult et al. (2013) described aPD1 antibodies directly activating B cells that had high PD1 expression. This mechanism was shown to be T cell independent and exclusive to peripheral B cell subsets. In addition, the authors noted that they did not observe any impact by aPD1 on production of class-switched antibody. In the Wang et al. (2019) study, the authors show that PD1-high B cells functionally suppress T cell activity, suggesting these B cells are a unique B regulatory cell subset. In contrast to the above studies, the B cell subsets in our tumor models did not show expression of Pdcd1 or express markers of B regulatory cells. Further, B cell activation by ICIs was dependent upon Tfh cell function and resembled those occurring in germinal center B cells. Finally, B cell activation by ICIs in our models was tied to increased class-switched antibody (IgG) production and activation of T cell subsets, as indicated by diminished numbers of memory T cells following B cell inhibition. Thus, our study reveals a distinct mechanism B cell activation while further uncovering the necessity of B cell and Tfh cell subsets in mediating ICI-induced anti-tumor responses.

Our findings also add context to prior studies that show B cells as prognostic in many cancers (Iglesia et al., 2016; Nzula et al., 2003; Shen et al., 2018). Here, we extend prognosis to therapeutic response with a new predictive gene signature. Building on these predictions, our study demonstrates B cells to be essential and multifunctional in ICI-driven anti-tumor responses via secreting antibody and helping T cell responses. The impact of B cell inhibition upon T cells is likely due to antigen presentation, as both central and effector memory $CD4^+$ subsets were impacted by inhibiting B cell function. This reduced $CD4^+$ T cell activity potentially explains the reduction in $CD8^+$ T cells, which rely on $CD4^+$ cells for activation and proliferation. Given the reduced efficacy of ICIs after depletion of T cell subsets, antigen presentation to amplify immune responses is likely a key function of B cells.

In addition to support of T cells, antibody generation by B cells was also key to ICI response in our GEMMs. Secreted IgG can elicit cytotoxicity by several mechanisms, such as complement or cellular cytotoxicity mediated by Fc-receptor activation (Vidarsson et al., 2014). These functions likely explain the loss of ICI efficacy we observed when using an Ig secretory-deficient mouse model or by blocking antibody activity using aCD16. The clonal restriction observed in BCR and/or IgG-repertoire profiling and serum IgG binding assays imply the antibodies induced by ICIs to be specific to model antigens. Together, these results depicting B cell mediation of anti-tumor responses through T cell activation and antibody generation present B cells, as well as Tfh cells, as an attractive cellular target to be leveraged to improve ICI therapy effectiveness.

Collectively, this study uncovers B cells and Tfh cells as direct mediators of ICI response in our mouse models, possibly in humans as well. Of note, scRNA-seq predicted a role for IL21 in B cell activation. While scRNA-seq may not prove which cytokines or receptors mediate a biological process, our follow-up studies verified that ICI induction of IL21 and Tfh cells activated B cells and class switching. Indeed, our analysis suggests these mechanisms may also extend to chemotherapy in TNBC patients and to trastuzumab response in $HER2^+$ breast cancer patients.

Figure 6. Immune Cell Depletion of Key Immune Cell Populations during Immune Checkpoint Therapy

(A) Survival for mice given aPD1/aCTLA4 therapy with aCD4 or aCD8 antibodies.

(B) 21-day acute response for mice given aPD1/aCTLA4 with aCD4 or aCD8 antibodies.

(C) Survival for mice given aPD1/aCTLA4 therapy with aCD19 or aCD20 antibodies.

(D) 21-day acute response for mice given aPD1/aCTLA4 with aCD19 or aCD20 antibodies.

(E) Flow cytometry results for T cell subsets after 7 days of aPD1/aCTLA4 therapy with or without aCD19-based B cell inhibition. In Kaplan-Meier plots, p value shows results of Log-rank (Mantel-Cox) tests. Boxplots show the mean and standard deviation. The p values are two-tailed from unmatched t tests.

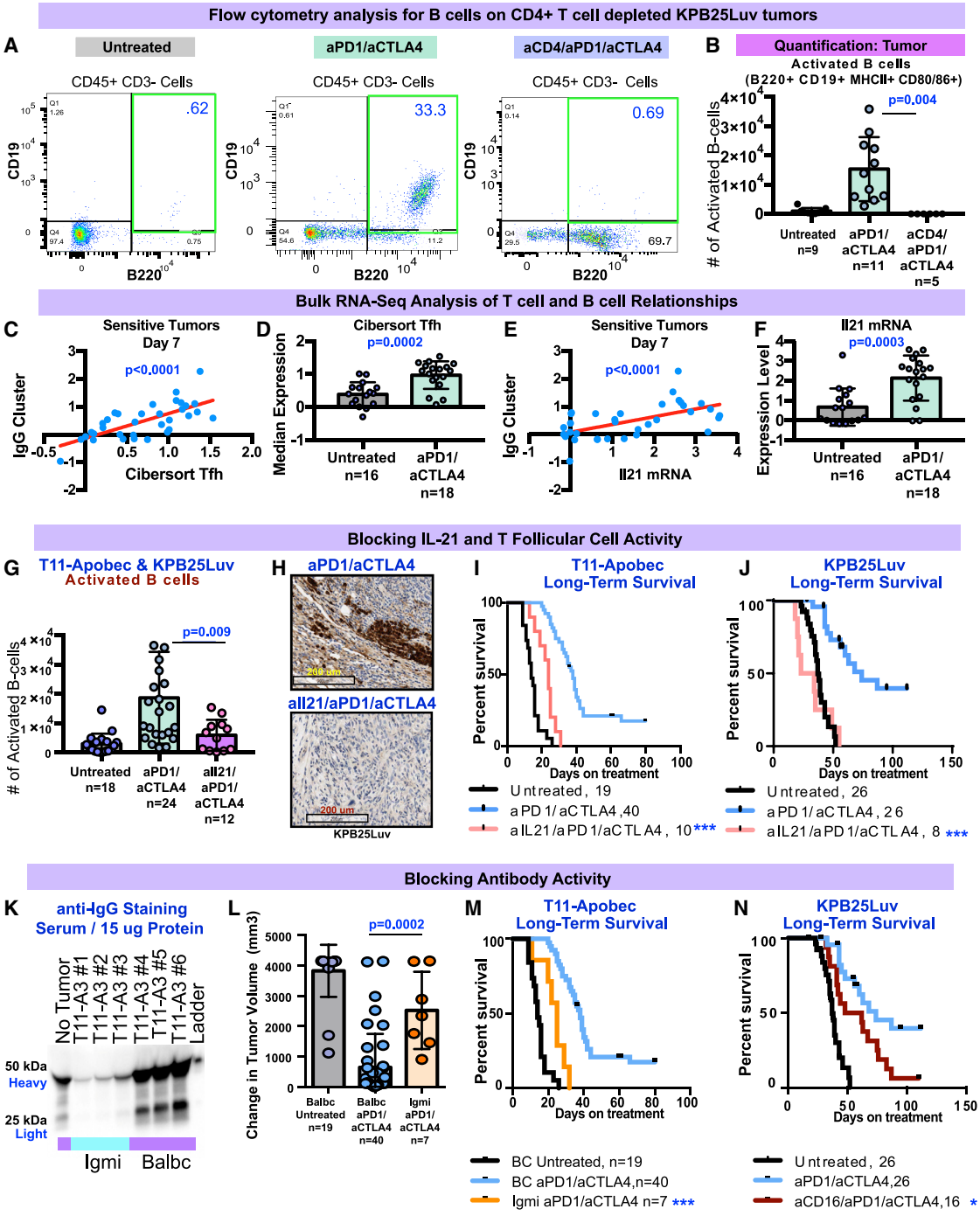

Figure 7. Testing B Cell Activation and IgG Functionality during Immune Checkpoint Therapy

(A) Flow cytometry for B cells in KPB25Luv tumors after 7 days of ICI and $CD4^+$ T cell depletion.

(B) Quantification of results from (A).

(C) x-y plot of IgG and CIBERSORT Tfh T cell signatures in mRNA-seq of sensitive tumors at day 7.

(D) Boxplot of CIBERSORT Tfh T cell signature levels in sensitive tumors (mRNA-seq) at day 7.

(E) x-y plot of IgG signature and Il21 mRNA in mRNA-seq of sensitive tumors at day 7.

(F) Boxplot of Il21 mRNA levels in sensitive tumors (mRNA-seq) at day 7.

(G) Flow cytometry results for activated B cells in T11-Apobec and KPB25Luv tumors during Tfh cell and IL21 blockade.

(H) IHC staining for IgG-kappa chain in KPB25Luv tumors during Tfh cell and IL21 blockade.

(I) Survival for T11-Apobec-bearing mice during ICI therapy and Tfh cell and IL21 blockade.

(legend continued on next page)

Moreover, our group has formerly noted that B cells are predictive of trastuzumab response (Tanioka et al., 2018). Taken together, these findings suggest the importance of the immune system across multiple distinct classes of anti-cancer agents and cancer types and where the active and coordinated engagement of both B cells and T cells portends good patient outcomes.

STAR★METHODS

Detailed methods are provided in the online version of this paper and include the following:

- KEY RESOURCES TABLE
- LEAD CONTACT AND MATERIALS AVAILABILITY
- EXPERIMENTAL MODEL AND SUBJECT DETAILS
  - Animal work
  - Antibody Regimens
  - *In vitro* cell line studies
- METHOD DETAILS
  - Flow cytometry
  - ELISA for IFNy detection
  - Immunohistochemistry
  - IgG-Binding Assay
  - Western blot
- QUANTIFICATION AND STATISTICAL ANALYSIS
  - RNA-seq analysis
  - Single Cell RNA-Seq
  - 5′ TCR/BCR Sequencing and Repertoire Analysis
  - External Gene Expression Data Analysis
  - Whole Exome Sequencing
- DATA AND CODE AVAILABILITY

SUPPLEMENTAL INFORMATION

Supplemental Information can be found online at https://doi.org/10.1016/j.cell.2019.10.028.

ACKNOWLEDGMENTS

We are grateful to the UNC Mouse Phase One Unit, Lineberger Comprehensive Cancer Center Immune Monitoring and Genomics Facility (IMGF); Janet Dow and the UNC Flow Cytometry Core Facility; Dr. Nana Feinberg, Yongjuan Xia, and Dr. Dawud Hilliard from UNC Translational Pathology and Histopathology labs; and the UNC Animal Studies Core for technical support and assistance. We thank Dr. Eran Andrechek for providing MMTV-PyMT tumors for RNA-sequencing. This work was supported by the following grants: NCI F32 Ruth L. Kirschstein National Research Service Award individual postdoctoral fellowship (Parent F32) CA210427 (to D.P.H.); NCI Breast SPORE program (P50-CA58223), RO1-CA148761, RO1-CA195740, the Breast Cancer Research Foundation, and Susan G. Komen SAC-160074 (to C.M.P.); Susan G. Komen Career Catalyst research grant (to B.G.V.); Susan G. Komen postdoctoral fellowship (PDF17479425) (to S.G.-R.); Corsorcio Centro de Investigación Biomédica en Red, thematic area for cancer (CIBERONC), Instituto de Salud Carlos III, Spain (to M.M.).

AUTHOR CONTRIBUTIONS

Conception and design, D.P.H. and C.M.P.; Generation of models, D.P.H.; Acquisition of data, D.P.H., A.T., C.G., N.X., J.P.G., S.G.-R., K.C.-E., S.C.V., K.R.M., S.L., M.M., and X.H.; Analysis and interpretation of data, D.P.H., N.X., K.R.M., X.H., S.C.V., C.G., S.G.-R., J.P.G., A.T., S.L., K.C.-E., J.S.S., and C.M.P.; Writing, review, and/or revision of the manuscript, D.P.H., N.X., A.T., C.G., J.P.G., S.G.-R., S.C.V., J.S.P., B.G.V., M.M., J.S.S., and C.M.P.; Administrative, technical, or material support, D.P.H., K.R.M., X.H., J.P.G., A.T., S.C.V., C.G., S.G.-R., D.M., J.F., J.S.P., B.G.V., M.M., J.S.S., and C.M.P.; Supervision, C.M.P.

DECLARATION OF INTERESTS

C.M.P is an equity stock holder and board of directors member of BioClassifier and GeneCentric Therapeutics. C.M.P and J.S.P. are also listed as inventors on patent applications on the Breast PAM50. C.M.P., B.G.V., and J.S.P. are equity stock holders in GeneCentric Therapeutics.

Received: January 29, 2019
Revised: September 12, 2019
Accepted: October 23, 2019
Published: November 14, 2019

REFERENCES

An, Y., Adams, J.R., Hollern, D.P., Zhao, A., Chang, S.G., Gams, M.S., Chung, P.E., He, X., Jangra, R., and Shah, J.S. (2018). Cdh1 and Pik3ca Mutations Cooperate to Induce Immune-Related Invasive Lobular Carcinoma of the Breast. Cell reports *25*, 702–714. e706.

Bindea, G., Mlecnik, B., Tosolini, M., Kirilovsky, A., Waldner, M., Obenauf, A.C., Angell, H., Fredriksen, T., Lafontaine, L., Berger, A., et al. (2013). Spatiotemporal dynamics of intratumoral immune cells reveal the immune landscape in human cancer. Immunity *39*, 782–795.

Bischof, J., and Ibrahim, S.M. (2016). bcRep: R package for comprehensive analysis of B cell receptor repertoire data. PLoS ONE *11*, e0161569.

Bolotin, D.A., Poslavsky, S., Mitrophanov, I., Shugay, M., Mamedov, I.Z., Putintseva, E.V., and Chudakov, D.M. (2015). MiXCR: software for comprehensive adaptive immunity profiling. Nat. Methods *12*, 380–381.

Budczies, J., Seidel, A., Christopoulos, P., Endris, V., Kloor, M., Győrffy, B., Seliger, B., Schirmacher, P., Stenzinger, A., and Denkert, C. (2018). Integrated analysis of the immunological and genetic status in and across cancer types: impact of mutational signatures beyond tumor mutational burden. OncoImmunology *7*, e1526613.

Bullard, J.H., Purdom, E., Hansen, K.D., and Dudoit, S. (2010). Evaluation of statistical methods for normalization and differential expression in mRNA-Seq experiments. BMC Bioinformatics *11*, 94.

Burns, M.B., Lackey, L., Carpenter, M.A., Rathore, A., Land, A.M., Leonard, B., Refsland, E.W., Kotandeniya, D., Tretyakova, N., Nikas, J.B., et al. (2013). APOBEC3B is an enzymatic source of mutation in breast cancer. Nature *494*, 366–370.

(J) Survival for KPB25Luv-bearing mice during ICI therapy and Tfh cell and IL21 blockade.
(K) Western blot for serum IgG in Igmi and Balbc mice with T11-Apobec tumors. The blue bars mark Igmi mouse sera; purple note Balbc sera.
(L) 21-day acute response in Igmi and Balbc control mice with T11-Apobec tumors.
(M) Survival of Igmi mice withT11-Apobec tumors and treated with aPD1/aCTLA4 therapy in contrast to Balbc controls.
(N) Survival in KPB25Luv tumor-bearing mice treated with ICI therapy or ICI therapy with CD16/32 blockade. In Kaplan-Meier plots, p values are from Log-rank (Mantel-Cox) tests. Boxplots show the mean and standard deviation. The p values are two-tailed from standard t tests. In x-y plots, p values were determined by linear regression analysis. The asterisks denote significance (***$p < 0.0001$, *$p < 0.05$).

Butler, A., Hoffman, P., Smibert, P., Papalexi, E., and Satija, R. (2018). Integrating single-cell transcriptomic data across different conditions, technologies, and species. Nature biotechnology *36*, 411.

Clark, E.A., and Ledbetter, J.A. (1994). How B and T cells talk to each other. Nature *367*, 425–428.

Cristescu, R., Mogg, R., Ayers, M., Albright, A., Murphy, E., Yearley, J., Sher, X., Liu, X.Q., Lu, H., and Nebozhyn, M. (2018). Pan-tumor genomic biomarkers for PD-1 checkpoint blockade–based immunotherapy. Science *362*, eaar3593.

de Hoon, M.J., Imoto, S., Nolan, J., and Miyano, S. (2004). Open source clustering software. Bioinformatics *20*, 1453–1454.

Dobin, A., Davis, C.A., Schlesinger, F., Drenkow, J., Zaleski, C., Jha, S., Batut, P., Chaisson, M., and Gingeras, T.R. (2013). STAR: ultrafast universal RNA-seq aligner. Bioinformatics *29*, 15–21.

Echavarria, I., López-Tarruella, S., Picornell, A.C., Garcia-Saenz, J.A., Jerez-Gilarranz, Y., Hoadley, K.A., Gomez, H., Moreno, F., Del Monte-Millan, M., and Márquez-Rodas, I. (2018). Pathological response in a triple negative breast cancer cohort treated with neoadjuvant carboplatin and docetaxel according to Lehmann's refined classification (clincanres: Clinical Cancer Research), 1912.2017.

Eksteen, B., Miles, A., Curbishley, S.M., Tselepis, C., Grant, A.J., Walker, L.S., and Adams, D.H. (2006). Epithelial inflammation is associated with CCL28 production and the recruitment of regulatory T cells expressing CCR10. J. Immunol. *177*, 593–603.

Esserman, L.J., Berry, D.A., Cheang, M.C., Yau, C., Perou, C.M., Carey, L., DeMichele, A., Gray, J.W., Conway-Dorsey, K., Lenburg, M.E., et al.; I-SPY 1 TRIAL Investigators (2012). Chemotherapy response and recurrence-free survival in neoadjuvant breast cancer depends on biomarker profiles: results from the I-SPY 1 TRIAL (CALGB 150007/150012; ACRIN 6657). Breast Cancer Res. Treat. *132*, 1049–1062.

Fan, C., Prat, A., Parker, J.S., Liu, Y., Carey, L.A., Troester, M.A., and Perou, C.M. (2011). Building prognostic models for breast cancer patients using clinical variables and hundreds of gene expression signatures. BMC Med. Genomics *4*, 3.

Heng, T.S., and Painter, M.W.; Immunological Genome Project Consortium (2008). The Immunological Genome Project: networks of gene expression in immune cells. Nat. Immunol. *9*, 1091–1094.

Herbst, R.S., Soria, J.-C., Kowanetz, M., Fine, G.D., Hamid, O., Gordon, M.S., Sosman, J.A., McDermott, D.F., Powderly, J.D., Gettinger, S.N., et al. (2014). Predictive correlates of response to the anti-PD-L1 antibody MPDL3280A in cancer patients. Nature *515*, 563–567.

Herschkowitz, J.I., Zhao, W., Zhang, M., Usary, J., Murrow, G., Edwards, D., Knezevic, J., Greene, S.B., Darr, D., Troester, M.A., et al. (2012). Comparative oncogenomics identifies breast tumors enriched in functional tumor-initiating cells. Proc. Natl. Acad. Sci. USA *109*, 2778–2783.

Hollern, D.P., Contreras, C.M., Dance-Barnes, S., Silva, G.O., Pfefferle, A.D., Xiong, J., Darr, D.B., Usary, J., Mott, K.R., and Perou, C.M. (2019). A mouse model featuring tissue-specific deletion of p53 and Brca1 gives rise to mammary tumors with genomic and transcriptomic similarities to human basal-like breast cancer. Breast Cancer Res. Treat. *174*, 143–155.

Hong, S., Zhang, Z., Liu, H., Tian, M., Zhu, X., Zhang, Z., Wang, W., Zhou, X., Zhang, F., and Ge, Q. (2018). B cells are the dominant antigen-presenting cells that activate naive CD4+ T cells upon immunization with a virus-derived nanoparticle antigen. Immunity *49*, 695–708.e694.

Huang, H., Liu, Y., Marron, J., and Huang, M.H. (2015). Package 'sigclust' (Department of Statistics and Operations Research, Lineberger Comprehensive Cancer Center, University of North Carolina).

Hundal, J., Carreno, B.M., Petti, A.A., Linette, G.P., Griffith, O.L., Mardis, E.R., and Griffith, M. (2016). pVAC-Seq: A genome-guided in silico approach to identifying tumor neoantigens. Genome Med. *8*, 11.

Iglesia, M.D., Vincent, B.G., Parker, J.S., Hoadley, K.A., Carey, L.A., Perou, C.M., and Serody, J.S. (2014). Prognostic B-cell signatures using mRNA-seq in patients with subtype-specific breast and ovarian cancer. Clin. Cancer Res. *20*, 3818–3829.

Iglesia, M.D., Parker, J.S., Hoadley, K.A., Serody, J.S., Perou, C.M., and Vincent, B.G. (2016). Genomic Analysis of Immune Cell Infiltrates Across 11 Tumor Types. J. Natl. Cancer Inst. *108*, djw144.

Jerry, D.J., Kittrell, F.S., Kuperwasser, C., Laucirica, R., Dickinson, E.S., Bonilla, P.J., Butel, J.S., and Medina, D. (2000). A mammary-specific model demonstrates the role of the p53 tumor suppressor gene in tumor development. Oncogene *19*, 1052–1058.

King, C. (2009). New insights into the differentiation and function of T follicular helper cells. Nat. Rev. Immunol. *9*, 757–766.

Kooreman, N.G., Kim, Y., de Almeida, P.E., Termglinchan, V., Diecke, S., Shao, N.-Y., Wei, T.-T., Yi, H., Dey, D., and Nelakanti, R. (2018). Autologous iPSC-based vaccines elicit anti-tumor responses in vivo. Cell stem cell *22*, 501–513.e507.

Le, D.T., Uram, J.N., Wang, H., Bartlett, B.R., Kemberling, H., Eyring, A.D., Skora, A.D., Luber, B.S., Azad, N.S., Laheru, D., et al. (2015). PD-1 blockade in tumors with mismatch-repair deficiency. N. Engl. J. Med. *372*, 2509–2520.

Li, H. (2013). Aligning sequence reads, clone sequences and assembly contigs with BWA-MEM. arXiv, arXiv:1303.3997, https://arxiv.org/abs/1303.3997.

Liberzon, A., Subramanian, A., Pinchback, R., Thorvaldsdóttir, H., Tamayo, P., and Mesirov, J.P. (2011). Molecular signatures database (MSigDB) 3.0. Bioinformatics *27*, 1739–1740.

Magurran, A.E. (2013). Measuring biological diversity (John Wiley & Sons).

Miller, L.D., Chou, J.A., Black, M.A., Chifman, J., Alistar, A., Putti, T., Zhou, X., Bedognetti, D., Hendrickx, W., and Pullikuth, A. (2016). Immunogenic subtypes of breast cancer delineated by gene classifiers of immune responsiveness (canimm: Cancer immunology research), 0149.2015.

Miyake, T., Nakayama, T., Naoi, Y., Yamamoto, N., Otani, Y., Kim, S.J., Shimazu, K., Shimomura, A., Maruyama, N., Tamaki, Y., and Noguchi, S. (2012). GSTP1 expression predicts poor pathological complete response to neoadjuvant chemotherapy in ER-negative breast cancer. Cancer Sci. *103*, 913–920.

Morganella, S., Alexandrov, L.B., Glodzik, D., Zou, X., Davies, H., Staaf, J., Sieuwerts, A.M., Brinkman, A.B., Martin, S., Ramakrishna, M., et al. (2016). The topography of mutational processes in breast cancer genomes. Nat. Commun. *7*, 11383.

Nelson, B.H. (2010). CD20+ B cells: the other tumor-infiltrating lymphocytes. J. Immunol. *185*, 4977–4982.

Network, C.G.A.; Cancer Genome Atlas Network (2012). Comprehensive molecular portraits of human breast tumours. Nature *490*, 61–70.

Newman, A.M., Liu, C.L., Green, M.R., Gentles, A.J., Feng, W., Xu, Y., Hoang, C.D., Diehn, M., and Alizadeh, A.A. (2015). Robust enumeration of cell subsets from tissue expression profiles. Nat. Methods *12*, 453–457.

Nolan, E., Savas, P., Policheni, A.N., Darcy, P.K., Vaillant, F., Mintoff, C.P., Dushyanthen, S., Mansour, M., Pang, J.-M.B., and Fox, S.B. (2017). Combined immune checkpoint blockade as a therapeutic strategy for BRCA1-mutated breast cancer. Science translational medicine *9*, eaal4922.

Nzula, S., Going, J.J., and Stott, D.I. (2003). Antigen-driven clonal proliferation, somatic hypermutation, and selection of B lymphocytes infiltrating human ductal breast carcinomas. Cancer Res. *63*, 3275–3280.

O'Garra, A. (1998). Cytokines induce the development of functionally heterogeneous T helper cell subsets. Immunity *8*, 275–283.

Parker, J.S., Mullins, M., Cheang, M.C., Leung, S., Voduc, D., Vickery, T., Davies, S., Fauron, C., He, X., Hu, Z., et al. (2009). Supervised risk predictor of breast cancer based on intrinsic subtypes. J. Clin. Oncol. *27*, 1160–1167.

Patro, R., Duggal, G., and Kingsford, C. (2015). Salmon: accurate, versatile and ultrafast quantification from RNA-seq data using lightweight-alignment. bioRxiv. https://doi.org/10.1101/021592.

Patro, R., Duggal, G., Love, M.I., Irizarry, R.A., and Kingsford, C. (2017). Salmon provides fast and bias-aware quantification of transcript expression. Nat. Methods *14*, 417–419.

Pauken, K.E., Sammons, M.A., Odorizzi, P.M., Manne, S., Godec, J., Khan, O., Drake, A.M., Chen, Z., Sen, D.R., Kurachi, M., et al. (2016). Epigenetic stability of exhausted T cells limits durability of reinvigoration by PD-1 blockade. Science *354*, 1160–1165.

Peggs, K.S., Quezada, S.A., Chambers, C.A., Korman, A.J., and Allison, J.P. (2009). Blockade of CTLA-4 on both effector and regulatory T cell compartments contributes to the antitumor activity of anti-CTLA-4 antibodies. J. Exp. Med. *206*, 1717–1725.

Pfefferle, A.D., Herschkowitz, J.I., Usary, J., Harrell, J.C., Spike, B.T., Adams, J.R., Torres-Arzayus, M.I., Brown, M., Egan, S.E., Wahl, G.M., et al. (2013). Transcriptomic classification of genetically engineered mouse models of breast cancer identifies human subtype counterparts. Genome Biol. *14*, R125.

Pfefferle, A.D., Agrawal, Y.N., Koboldt, D.C., Kanchi, K.L., Herschkowitz, J.I., Mardis, E.R., Rosen, J.M., and Perou, C.M. (2016). Genomic profiling of murine mammary tumors identifies potential personalized drug targets for p53-deficient mammary cancers. Dis. Model. Mech. *9*, 749–757.

Pfefferle, A.D., Darr, D.B., Calhoun, B.C., Mott, K.R., Rosen, J.M., and Perou, C.M. (2019). The MMTV-Wnt1 murine model produces two phenotypically distinct subtypes of mammary tumors with unique therapeutic responses to an EGFR inhibitor. Disease Models & Mechanisms, dmm. 037192.

Qin, S., Rottman, J.B., Myers, P., Kassam, N., Weinblatt, M., Loetscher, M., Koch, A.E., Moser, B., and Mackay, C.R. (1998). The chemokine receptors CXCR3 and CCR5 mark subsets of T cells associated with certain inflammatory reactions. J. Clin. Invest. *101*, 746–754.

Rizvi, N.A., Hellmann, M.D., Snyder, A., Kvistborg, P., Makarov, V., Havel, J.J., Lee, W., Yuan, J., Wong, P., Ho, T.S., et al. (2015). Cancer immunology. Mutational landscape determines sensitivity to PD-1 blockade in non-small cell lung cancer. Science *348*, 124–128.

Sade-Feldman, M., Yizhak, K., Bjorgaard, S.L., Ray, J.P., de Boer, C.G., Jenkins, R.W., Lieb, D.J., Chen, J.H., Frederick, D.T., and Barzily-Rokni, M. (2018). Defining T Cell States Associated with Response to Checkpoint Immunotherapy in Melanoma. Cell *175*, 998–1013. e1020.

Saunders, C.T., Wong, W.S., Swamy, S., Becq, J., Murray, L.J., and Cheetham, R.K. (2012). Strelka: accurate somatic small-variant calling from sequenced tumor-normal sample pairs. Bioinformatics *28*, 1811–1817.

Schmid, P., Adams, S., Rugo, H.S., Schneeweiss, A., Barrios, C.H., Iwata, H., Diéras, V., Hegg, R., Im, S.-A., Shaw Wright, G., et al.; IMpassion130 Trial Investigators (2018). Atezolizumab and nab-paclitaxel in advanced triple-negative breast Cancer. N. Engl. J. Med. *379*, 2108–2121.

Selitsky, S.R., Mose, L.E., Smith, C.C., Chai, S., Hoadley, K.A., Dittmer, D.P., Moschos, S.J., Parker, J.S., and Vincent, B.G. (2019). Prognostic value of B cells in cutaneous melanoma. Genome Med. *11*, 36.

Sharma, P., and Allison, J.P. (2015). The future of immune checkpoint therapy. Science *348*, 56–61.

Shen, M., Wang, J., and Ren, X. (2018). New insights into tumor-infiltrating B lymphocytes in breast cancer: clinical impacts and regulatory mechanisms. Front. Immunol. *9*, 470.

Smid, M., Rodríguez-González, F.G., Sieuwerts, A.M., Salgado, R., Prager-Van der Smissen, W.J., Vlugt-Daane, M.V., van Galen, A., Nik-Zainal, S., Staaf, J., Brinkman, A.B., et al. (2016). Breast cancer genome and transcriptome integration implicates specific mutational signatures with immune cell infiltration. Nat. Commun. *7*, 12910.

Tanioka, M., Fan, C., Parker, J., Hoadley, K., Hu, Z., Li, Y., Hyslop, T., Pitcher, B., Soloway, M., and Spears, P. (2018). Integrated Analysis of RNA and DNA from the Phase III Trial CALGB 40601 Identifies Predictors of Response to Trastuzumab-Based Neoadjuvant Chemotherapy in HER2-Positive Breast Cancer. Clinical cancer research: an official journal of the American Association for Cancer Research.

Taylor, N.A., Vick, S.C., Iglesia, M.D., Brickey, W.J., Midkiff, B.R., McKinnon, K.P., Reisdorf, S., Anders, C.K., Carey, L.A., Parker, J.S., et al. (2017). Treg depletion potentiates checkpoint inhibition in claudin-low breast cancer. J. Clin. Invest. *127*, 3472–3483.

Thibult, M.-L., Mamessier, E., Gertner-Dardenne, J., Pastor, S., Just-Landi, S., Xerri, L., Chetaille, B., and Olive, D. (2013). PD-1 is a novel regulator of human B-cell activation. Int. Immunol. *25*, 129–137.

Tischler, G., and Leonard, S. (2014). biobambam: tools for read pair collation based algorithms on BAM files. Source Code Biol. Med. *9*, 13.

Topalian, S.L., Hodi, F.S., Brahmer, J.R., Gettinger, S.N., Smith, D.C., McDermott, D.F., Powderly, J.D., Carvajal, R.D., Sosman, J.A., Atkins, M.B., et al. (2012). Safety, activity, and immune correlates of anti-PD-1 antibody in cancer. N. Engl. J. Med. *366*, 2443–2454.

Tsavaris, N., Kosmas, C., Vadiaka, M., Kanelopoulos, P., and Boulamatsis, D. (2002). Immune changes in patients with advanced breast cancer undergoing chemotherapy with taxanes. Br. J. Cancer *87*, 21–27.

Tumeh, P.C., Harview, C.L., Yearley, J.H., Shintaku, I.P., Taylor, E.J., Robert, L., Chmielowski, B., Spasic, M., Henry, G., Ciobanu, V., et al. (2014). PD-1 blockade induces responses by inhibiting adaptive immune resistance. Nature *515*, 568–571.

Turner, L.H., Kinder, J.M., Wilburn, A., D'Mello, R.J., Braunlin, M.R., Jiang, T.T., Pham, G., and Way, S.S. (2017). Preconceptual Zika virus asymptomatic infection protects against secondary prenatal infection. PLoS Pathog. *13*, e1006684.

Tusher, V.G., Tibshirani, R., and Chu, G. (2001). Significance analysis of microarrays applied to the ionizing radiation response. Proc. Natl. Acad. Sci. USA *98*, 5116–5121.

Van Allen, E.M., Miao, D., Schilling, B., Shukla, S.A., Blank, C., Zimmer, L., Sucker, A., Hillen, U., Foppen, M.H.G., Goldinger, S.M., et al. (2015). Genomic correlates of response to CTLA-4 blockade in metastatic melanoma. Science *350*, 207–211.

Vidarsson, G., Dekkers, G., and Rispens, T. (2014). IgG subclasses and allotypes: from structure to effector functions. Front. Immunol. *5*, 520.

Vogelzang, A., McGuire, H.M., Yu, D., Sprent, J., Mackay, C.R., and King, C. (2008). A fundamental role for interleukin-21 in the generation of T follicular helper cells. Immunity *29*, 127–137.

Waisman, A., Kraus, M., Seagal, J., Ghosh, S., Melamed, D., Song, J., Sasaki, Y., Classen, S., Lutz, C., Brombacher, F., et al. (2007). IgG1 B cell receptor signaling is inhibited by CD22 and promotes the development of B cells whose survival is less dependent on Ig α/β. J. Exp. Med. *204*, 747–758.

Wang, S., Jia, M., He, Z., and Liu, X.-S. (2018). APOBEC3B and APOBEC mutational signature as potential predictive markers for immunotherapy response in non-small cell lung cancer. Oncogene *37*, 3924–3936.

Wang, X., Wang, G., Wang, Z., Liu, B., Han, N., Li, J., Lu, C., Liu, X., Zhang, Q., Yang, Q., and Wang, G. (2019). PD-1-expressing B cells suppress $CD4^+$ and $CD8^+$ T cells via PD-1/PD-L1-dependent pathway. Mol. Immunol. *109*, 20–26.

Wein, L., Luen, S.J., Savas, P., Salgado, R., and Loi, S. (2018). Checkpoint blockade in the treatment of breast cancer: current status and future directions. Br. J. Cancer *119*, 4–11.

Wherry, E.J., and Kurachi, M. (2015). Molecular and cellular insights into T cell exhaustion. Nat. Rev. Immunol. *15*, 486–499.

Zhang, X., Lan, Y., Xu, J., Quan, F., Zhao, E., Deng, C., Luo, T., Xu, L., Liao, G., Yan, M., et al. (2019). CellMarker: a manually curated resource of cell mavrkers in human and mouse. Nucleic Acids Res. *47* (D1), D721–D728.

STAR★METHODS

KEY RESOURCES TABLE

REAGENT or RESOURCE	SOURCE	IDENTIFIER
Antibodies		
Anti-mouse PD1 (clone RMP1-14)	Bioxcel	Cat: BE0146; RRID: AB_10949053
Anti-mouse CTLA4 (clone 9D9)	Bioxcel	Cat: BE0164; RRID: AB_10949609
Anti-mouse CD4 (clone GK1.5)	Bioxcel	Cat: BE0003-1; RRID: AB_1107636
Anti-mouse CD8a (clone 53-6.7)	Bioxcel	Cat: BE0004-1; RRID: AB_1107671
Anti-mouse CD19 (clone 1D3)	Bioxcel	Cat: BE0150; RRID: AB_10949187
Anti-mouse CD16/32 (clone 2.4G2)	Bioxcel	Cat: BE0307; RRID: AB_2736987
Anti-mouse CD20 (clone SA271G2)	Biolegend	Cat: 152104; RRID: AB_2629619
Anti-mouse IL21 (clone FFA21)	Thermofisher	Cat: 16-7211-82; RRID: AB_1963610
Mouse IgG2b Isotype Control (clone MPC-11)	Bioxcel	Cat: BE0086; RRID: AB_1107791
Rat IgG2a Isotype Control (clone 2A3)	Bioxcel	Cat: BE0089; RRID: AB_1107769
Anti-mouse CD45, eFluor 450 (clone 30-F11)	Thermofisher	Cat: 48-0451-82; RRID: AB_1518806
Anti-mouse B220 (CD45R), BV785 (clone RA3-6B2)	Biolegend	Cat: 103246; RRID: AB_2563256
Anti-mouse CD19, APC-H7 (clone 1D3)	BD Biosciences	Cat: 560245; AB_1645233
Anti-mouse CD20, PE (clone AISB12)	Thermofisher	Cat: 12-0201-80; RRID: AB_1210737
Anti-mouse I-A/I-E (MHC II); BV5210 (clone M5/114.15.2)	Biolegend	Cat: 107636; RRID: AB_2734168
Anti-mouse CD80; APC (clone 16-10A1)	Biolegend	Cat: 104714; RRID: AB_313135
Anti-mouse CD86; Fitc (clone GL1)	BD Biosciences	Cat: 561962; RRID: AB_10896136
Anti-mouse CD16/32; Fitc (clone 2.4G2)	BD Biosciences	Cat: 553144; RRID: AB_394659
Anti-mouse CD3; Fitc (clone 17A2)	Thermofisher	Cat: 11-0032-82; RRID: AB_2572431
Anti-mouse CD4; BV510 (clone GK1.5)	Biolegend	Cat: 100449; RRID: AB_2564587
Anti-mouse CD8a; APH-H7 (clone 53-6.7)	BD Biosciences	Cat: 560182; RRID: AB_1645237
Anti-mouse CD44; PerCP-Cyanine5.5 (clone IM7)	Thermofisher	Cat: 45-0441-82; RRID: AB_925746
Anti-mouse CD62L; APC (clone MEL-14)	BD Biosciences	Cat: 553152; RRID: AB_398533
Anti-mouse FOXP3; PE (clone FJK-16 s)	Thermofisher	Cat: 12-5773-82; RRID: AB_465936
Anti-mouse CD20; (clone SP32)	Abcam	Cat: ab64088; RRID: AB_1139386
Anti-mouse B220/CD45R; (clone RA3-6B2)	Abcam	Cat: ab64100; RRID: AB_1140036
Anti-mouse CD3;DAB (polyclonal)	Abcam	Cat: ab5690; RRID: AB_305055
Anti-mouse IgG-Kappa; (clone RM103)	Abcam	Cat: ab190484; RRID:AB_2811042
Anti-mouse IgM, HRP (polyclonal)	Biorad	Cat: 5276-2504; RRID: AB_619904
Anti-mouse IgG1, HRP (polyclonal)	Biorad	Cat: OBT1508P; RRID: AB_619901
Anti-rabbit IgG Cross-adsorbed, Unconjugated (polyclonal)	Thermofisher	Cat: 31213; RRID: AB_228376
Anti-mouse IgG, Alexa Fluor 488 (polyclonal)	Thermofisher	Cat: A-11001; RRID: AB_2534069
Anti-rabbit IgG, HRP	Ventana Medical Systems	Cat: 760-4311; RRID: AB_2811043
Biological Samples		
2336R Tumor Transplant Line 2153L Tumor Transplant Line 2225L Tumor Transplant Line 2224L Tumor Transplant Line 9263-3F Tumor Transplant Line	Tp53−/− Tumors (Jerry et al., 2000; Herschkowitz et al., 2012) This paper Perou Lab	N/A

(*Continued on next page*)

Continued

REAGENT or RESOURCE	SOURCE	IDENTIFIER
Chemicals, Peptides, and Recombinant Proteins		
Fixable viability stain 700	BD Biosciences	Cat: 564997
Rodent Decloaker, 10XPretreatment Reagent	Biocare Medical	Cat: RD913 L, M
Critical Commercial Assays		
TruSeq Stranded mRNA	Illumina	TruSeq Stranded mRNA Library Prep (48 Samples) 20020594
Chromium Single Cell 3′ Reagent Kits	10x Genomics	Chromium Single Cell 3′ Library & Gel Bead Kit v2, PN-120237 Single Cell 3′ Chip Kit v2 PN-120236 i7 Multiplex Kit PN-120262
MACS Tumor Dissociation Kit, mouse	Miltenyi Biotech	Tumor dissociation kit # 130-096-730
ChromoMap DAB kit	Ventana Medical Systems	Cat: 760-159
QIAGEN DNeasy blood and tissue kit	QIAGEN	Cat: 69506
QIAGEN RNeasy Mini Kit	QIAGEN	Cat: 74104
Mouse IFN-γ ELISA Kit II	BD Biosciences	Cat: 558258
SMARTer Mouse BCR IgG H/K/L Profiling Kit	Takara	Cat: 634422
SMARTer Mouse TCR a/b Profiling Kit	Takara	Cat: 634402
Agilent Sure Select XT kit	Agilent	Cat: G9611B
Agilent SureSelect Mouse All Exon	Agilent	Cat: 5190-4642
eBioscience FoxP3 staining kit	Thermofisher	Cat: 00-5523-00
Deposited Data		
Raw and normalized data; microarray	Miyake et al., 2012	GEO: GSE32646
Raw and normalized data; microarray	Esserman et al., 2012	GEO: GSE22226
Raw data; RNA-seq	Tanioka et al., 2018	GEO: GSE116335
Raw data; RNA-seq	Van Allen et al., 2015	SRA: DbGAP phs000452.v2.p1
Raw data; RNA-seq	Echavarria et al., 2018	https://doi.org/10.1158/1078-0432.CCR-17-1912
Raw and normalized data; single-cell RNA-seq	Sade-Feldman et al., 2018	GEO: GSE120575
Raw data and normalized data; RNA-seq	This paper	GEO: GSE124821; PRJNA506275
Raw data and normalized data; RNA-seq	Pfefferle et al., 2019	GEO: GSE118164
Raw and normalized data; scRNA-seq	This paper	GEO: GSE136206
Experimental Models: Cell Lines		
KPB25L-Parent KPB25Luv KPB-Apobec	K14-Cre;Tp53 f/f Brca1 f/f Parent model-(Hollern et al., 2019) Mutagenized- This paper Perou Lab	NA
T11- Parent T11-uv T11-Apobec	Tp53−/− Parent model-(Jerry et al., 2000; Herschkowitz et al., 2012) Mutagenized- This paper Perou Lab	NA
Experimental Models: Organisms/Strains		
Mouse: FVB/NJ	The Jackson Laboratory	JAX: 001800
Mouse: Balb/cJ	The Jackson Laboratory	JAX: 000651
Mouse: Igmi	Waisman et al., 2007 Serody lab- UNC	NA
Oligonucleotides		
Igmi Mice Genotyping Primers: 5′GAGACGAGGGGGAAGACATTTG3′, 5′CCTTCCTCCTACCCTACA AGCC3′	Waisman et al., 2007	NA

(*Continued on next page*)

Continued

REAGENT or RESOURCE	SOURCE	IDENTIFIER
Recombinant DNA		
Apobec3 plasmid	VectorBuilder	VB170110-1098xwd
Software and Algorithms		
Seurat (version 2.3.4)	Butler et al., 2018	https://github.com/satijalab/seurat
MIXCR (version 2.1.9-6)	Bolotin et al., 2015	https://github.com/milaboratory/mixcr/
R (3.5.1)	R Core Team	https://www.R-project.org/
R Studio	R Studio	https://www.rstudio.com
STAR aligner	Dobin et al., 2013	https://github.com/alexdobin/STAR
SALMON	Patro et al., 2015 Patro et al., 2017	https://combine-lab.github.io/salmon/
Picard	Broad Institute	https://broadinstitute.github.io/picard/
Cluster 3.0	de Hoon et al., 2004	http://bonsai.hgc.jp/~mdehoon/software/cluster/software.htm
Java TreeView	NA	http://bonsai.hgc.jp/~mdehoon/software/cluster/software.htm
FlowJo (version 10)	FlowJo	https://www.flowjo.com/solutions/flowjo/downloads/
CellRanger (version 3.0.2)	10X Genomics	https://support.10xgenomics.com/single-cell-gene-expression/software/pipelines/latest/what-is-cell-ranger
pVAC seq	Hundal et al., 2016	https://pvac-seq.readthedocs.io/en/latest/
IMMGEN MyGeneSet	Heng et al., 2008	http://rstats.immgen.org/MyGeneSet_New/index.html
IGV	Broad Institute	http://software.broadinstitute.org/software/igv/userguide
Vegan	vegan: Community Ecology Package	https://cran.r-project.org/web/packages/vegan/vegan.pdf
GraphPad Prism	GraphPad Software	https://www.graphpad.com/
Significance Analysis of Microarrays	Tusher et al., 2001	https://CRAN.R-project.org/package=samr
SAMtools		http://www.htslib.org
Biobambam	Tischler and Leonard, 2014	https://github.com/gt1/biobambam
BWA mem	Li 2013	http://bio-bwa.sourceforge.net
Strelka	Saunders et al., 2012	https://github.com/Illumina/strelka
SigClust	Huang et al., 2015	https://cran.r-project.org/web/packages/sigclust/index.html
Other		
Matrigel® Basement Membrane Matrix	Corning	Cat: 354234
HUMEC READY MEDIUM-(With supplement)	Life Technologies	Cat: 12752010
RPMI 1640	Life Technologies	Cat: 11875093
DMEM	Life Technologies	Cat: 11995065
Discovery antibody diluent	Ventana Medical Systems	Cat: 760-108
FUGENE Transfection reagent	Promega	Cat: E2311

LEAD CONTACT AND MATERIALS AVAILABILITY

Further information and requests for materials may be directed to the corresponding author Charles M Perou. (cperou@med.unc.edu). Key reagents and tumor lines are available and can be obtained by contacting Charles M Perou. (cperou@med.unc.edu).

EXPERIMENTAL MODEL AND SUBJECT DETAILS

Animal work

All animal work was conducted according to IACUC guidelines. All mice were allowed to mature to 12 weeks prior to injection. All tumor studies used female mice. FVB and Balbc mice were ordered from Jackson Laboratories. Tumor transplants were syngeneic; KPB25L parental and mutagenized lines were orthotopically injected in FVB recipients and TP53$^{-/-}$ models (see Table 1) were orthotopically injected into Balbc recipients. To determine endogenous IgG functionality, mice genetically engineered to be deficient in Ig secretion (Igmi mice) were used with T11-Apobec tumors(Waisman et al., 2007). Mice were bred to homozygosity; genotyping primers: 5′GAGACGAGGGGGAAGACATTTG3′,5′CCTTCCTCCTACCCTACA AGCC3′. Injections were done as single cell suspensions of approximately 100,000 cells in Matrigel to the number four mammary gland. KPB25L, KPB25Luv, KPB25L-Apobec, T11, T11-UV, and T11-Apobec exist as cell lines. Parental lines are derived from transplantable tumors, which are present in the Figure 1 cluster analysis. Other models are tumor transplant lines and were digested with the Miltenyi tumor dissociation kit to establish cell suspensions (130-096-730). Mice were examined 2-3 times weekly for tumor outgrowth and upon tumor diameter of 5mm, mice were randomly assigned to treatment or control groups. Caliper measurement continued at a 2-3 per week frequency until end-stage (tumor diameter = 20mm).

Antibody Regimens

Antibody was delivered using 100ul volumes and injected intraperitoneally bi-weekly for the following: aCTLA4 (125 ug, bioxcel BE0164), aPD1 (10mg/kg, bioxcel BE0146), anti-CD19 (400ug, bioxcel BE0150), aCD8 (500ug, bioxcel BE0004), aCD4 (500ug, bioxcel BE0003), and aCD16/32 (500ug, bioxcel, BE0307), aIL21 (100ug, ThermoFisher, 16-7211-82). Mice received one tail vein injection of aCD20 (Ultra-LEAF Purified anti-mouse CD20, item 152104, reported depletion of 30 or more days) and then given biweekly doses of the aPD1/aCTLA4 combination therapy. Depletion was confirmed by flow-cytometry in the context of combination anti-PD1/anti-CTLA4 treatment for 7 days.

In vitro cell line studies

T11 cell lines and mutagenized versions were culture in GIBCO RPMI media supplemented with 5% fetal bovine serum and 1X penn-strep. KPB25L cell lines and mutagenized versions were cultured in GIBCO HUMEC media with supplement. Media was supplemented with 5% fetal bovine serum and 1X penn-strep. To generate Apobec3 overexpressing lines, we purchased a vector that overexpresses the mouse Apobec3 ORF under the control of the EF1A promoter from vectorbuilder (VB170110-1098xwd). This isoform lacks exon 5, thus allowing Apobec3 overexpression to be determined by examining read alignments spanning exon 4 and exon 6 using sashimi plots on IGV. Cells were stably transfected using FUGENE. To allow for the accumulation of mutations, KPB25L-Apobec cells were cultured for 1 month prior to whole exome sequencing and experimental studies (*in vivo* and *in vitro*). Similarly, T11-Apobec cells were cultured for two months prior to whole exome sequencing and experimentation. The matching parental lines (T11, 2 months; KPB25L, 1 month) were kept in culture for the same amount of time prior to sequencing to control for other mutation sources (i.e.- p53 loss, BRCA1 loss). For mutagenization by ultraviolet light, exposure was received by placing cells cultured in 10cm plate (lid removed) underneath a germicidal UV lamp that emits 253.7 nm lightwaves and runs at 100mw per cm^2 at maximum to 40 mw per cm^2 at minimum. Exposure was done in 30 s increments. Total exposure time for KPB25Luv was 1 min and 30 s and 5 min for T11-UV. Cells were allowed to recover to 70%–90% confluency and then cultured for 10-14 days prior further experimentation. To measure cell proliferation, we performed a cell counting experiment in triplicate. On day 0, cells were seeded and then cells were counted the next 3 days using trypan blue stain and countess cell counter.

METHOD DETAILS

Flow cytometry

Tumors were digested into single suspensions using the Miltenyi tumor dissociation kit (130-096-730) and Miltenyi gentleMACs dissociator. Spleen was placed in DMEM for gentleMACS dissociation. Cells were washed three times and resuspended in PBS diluted live/dead staining dye (Fixable Viability Stain 700, BD) for 35 min on ice followed by washing with PBS. Fc Block (clone 2.4G2; Bioxcell) diluted with staining buffer (PBS with 10% FCS) was then used for blocking for 20 min on ice. Fluorochrome labeled antibodies diluted with staining buffer were added and staining was continued for 40 min on ice. After a washing step, cells were fixed/stored in a 1% PFA solution until analysis. When staining for T cells, stained cells were then permeabilized for FoxP3 staining using eBioscience FoxP3 staining kit according to manufacturer's instructions and stained with anti-Foxp3 antibody. Fluorochrome labeled antibodies are listed in the methods table. T cells staining antibodies were: anti-CD45, CD3, CD4, CD8, CD62L, CD44, Foxp3. The fluorochrome labeled antibodies for B cells staining were: anti-CD45, CD19, CD20, B220, MHCII, CD80, CD86. Flow cytometry sample acquisition was performed on a LSRFortessa (BD), and analysis was performed using FlowJo software (TreeStar). The gating strategy is as illustrated in Figure S4. Cell counts were quantified as follows.

$$\text{Gated cell number} = \frac{\text{Events of gated cells}}{\text{Events of total live cells}} \times 10^6$$

ELISA for IFNy detection

An Elisa was performed according to manufacturer instructions using the Mouse IFN-γ ELISA Kit II (Cat: 558258, BD Biolegend) to compare T11 parental and T11-Apobec serum from non-treated mice harboring these respective tumors. ELISA plates were scanned on Synergy2 Microplate Reader (Biotek Instruments Inc). Standards and samples absorbance and optical density were analyzed using Gen5 Data Analysis software (Biotek Instruments Inc).

Immunohistochemistry

Immunohistochemistry used paraffin embedded tumors from mice that received treatment for 7 days. The untreated control samples were matched time points from mice bearing tumors that had reached 5mm and collected 7 days later. All immunohistochemistry and embedding were conducted by the UNC Animal Histopathology Core. The IgG staining used a Rabbit anti-mouse monoclonal [RM103] to IgG-Kappa light chain (ab190484). The aCD20 stain used ab64088. The anti-B220 staining used ab64100. The aCD3 staining used ab5690. Antigen retrieval used Ventana's CC1 (pH 8.5), for 40 min @ 95°C and given a block (Rodent Decloaker 10X, Biocare, BM#RD913L) for 1 h, followed by a peroxidase block for 12 min. Next, primary antibody diluent (1:700) was added for 1 h at room temperature using Discovery AB Diluent (760-108), followed by a post-peroxidase block for 12 min. Secondary antibody was added (Discovery OmniMap anti Rabbit HRP, 760-4311, Ready to Use) for 32 min at room temperature. The samples were treated with DAB, Hematoxylin II for 12 min, and then Bluing Reagent for 4 min. Slide staining used Ventana's Discovery Ultra Automated IHC staining system.

IgG-Binding Assay

The IgG binding assay was based upon an established protocol(Kooreman et al., 2018). Tumor bearing mice were euthanized following 7 days of therapy (or time matched in non-treated control). Whole blood was collected by cardiac puncture, blood was allowed to coagulate, and tubes were spun for 10 min at 4°C. The supernatant was collected to provide a source of serum for IgG binding tests. Cells were washed three times using centrifugation and PBS and resuspended in 100 μL PBS buffer with the addition of 2 μL of serum. Incubation was one on ice for 45 min. On target testing used serum that came from a KPB25Luv tumor bearing mouse on KPB25Luv cells from culture or serum from T11-apobec bearing mouse on T11-Apobec cells from tissue culture. Off-target binding was assessed by cross reactivity with opposite combinations of the aforementioned cells. Since T11-Apobec cells showed high cross-reactivity a pre-absorption protocol was followed to remove autoantibodies from the assay. Pre-absorption was done by incubating serum with the T11 parental cell line for 45 min on ice. Cells were then centrifuged and the supernatant collected and then incubated with T11-apobec cells for 45 min on ice. Background was assessed using the antibody. To detect IgG binding to cells, a FITC-tagged anti-mouse IgG (Thermofisher Scientific) was used. Background was assessed by using an isotype control IgG antibody.

Western blot

Mouse serum was harvested from tumor bearing Igmi and Balbc mice by cardiac puncture. In addition, serum was obtained from non-tumor bearing mice. Serum protein was quantified using DC Protein Assay (Bio-Rad, Hercules CA) and all samples were diluted to equal concentration using water. Samples were separate by electrophoresis on 4%–15% Tris-Glycine polyacrylamide gels (Bio-Rad), transferred to Hybond® PVDF membrane (MilliporeSigma, St. Louis MO), blocked for 1 h at room temperature in 5% BSA (MilliporeSigma) in TBS with 0.05% Tween-20. The membrane was incubated with either IgG1 HRP-conjugated (OBT1508P) or IgM MU CHAIN HRP-conjugated (5276-2504) antibody (Bio-Rad) for 2 h while rocking at room temperature. The membrane was washed three times in TBS with 0.05% Tween-20 and exposed to SuperSignal chemiluminescent substrate (ThermoScientific Scientific, Waltham MA). The membrane was visualized using the ChemiDoc MP Imaging System (Bio-Rad).

QUANTIFICATION AND STATISTICAL ANALYSIS

RNA-seq analysis

mRNA was isolated using the QIAGEN RNeasy kit according to manufacturer protocol. mRNA quality was assessed using the Agilent Bioanalyzer and libraries for mRNA-seq made using total RNA and the Illumina TruSeq mRNA sample preparation kit. Paired end (2x50bp) sequencing was performed on the Illumina HiSeq 2000/2500 sequencer at the UNC High Throughput Sequencing Facility. Resulting fastq files were aligned to the mouse mm10 reference genome using the STAR aligner algorithm(Dobin et al., 2013). Resulting BAM files were sorted and indexed using Samtools and quality control was performed using Picard. Transcript read counts were determined was performed using Salmon(Patro et al., 2015). Genes with no reads across any of the samples were removed. Salmon gene-level counts upper quartile normalized(Bullard et al., 2010). Genes with an average expression less than 10 were filtered from the dataset. Genes were log2 transformed using Cluster 3.0 and zeros were preserved for signature analysis. Data was then median centered and column standardized to establish the matrix in working form for statistical analyses. Hierarchical clustering was done using Cluster 3.0(de Hoon et al., 2004) and viewed in Java Tree View. Supervised gene expression analyses were performed using Significance Analysis of Microarrays (Tusher et al., 2001) and an FDR of 5%. Gene expression signatures were calculated as the median expression of all the genes in the signature as published(Fan et al., 2011). In signatures analysis, mouse genes were converted to human using BioMart. Univariate and multivariate analyses were performed using standardized signature scores in

R-studio using logistic regression. Boxplots and KM plots were generated in graph pad prism. Sashimi plots demonstrating Apobec3 overexpression were done using IGV. All murine RNaseq data, totaling 290 samples, have been deposited into the NCBI Gene Expression Omnibus (GEO): GSE124821, GSE118164 (MMMTV-Wnt tumors [Pfefferle et al., 2019]), the CDH1/PIK3Ca tumors were published and included as RNA-seq data in this study (An et al., 2018), and raw sequence files are in NCBI Sequence Read Archive (SRA): PRJNA506275.

Single Cell RNA-Seq

Single cell suspensions were generated using the Miltenyi mouse tumor dissociation kit and a gentleMACS tissue dissociator. Single cell suspensions were input to a 10x Genomics Chromium machine to establish single-cell gel beads in emulsion (GEMs) for directed retrieval of approximately 5000-10000 cells. Single-cell RNA-Seq libraries were primed using the following Single Cell 3′ Reagent Kits v2: Chromium Single Cell 3′ Library & Gel Bead Kit v2, PN-120237; Single Cell 3′ Chip Kit v2 PN-120236 and i7 Multiplex Kit PN-120262'' (10x Genomics). Protocols were performed as directed in the Single Cell 3′ Reagent Kits v2 User Guide (Manual Part # CG00052 Rev A). Libraries were sequenced on an Illumina HiSeq 4000 as 2 × 150 paired-end reads. The Cell Ranger Single Cell Software Suite, version 3.0.2 was used for de-multiplexing, barcode ad UMI processing, and single-cell 3′ gene counting. Specific details and instructions to run Cell Ranger can be found at: https://support.10xgenomics.com/single-cell-gene-expression/software/pipelines/latest/what-is-cell-ranger). Reads were mapped to the mm10 genome.

Cell ranger output and single cell RNA-seq data were analyzed using the R-package Seurat version 2.3.4. Here quality control parameters were utilized to filter dead-cells, doublets, and cells without the minimal number of expressed genes. Preprocessing for clustering and marker gene analysis was as follows. Raw UMI counts were normalized using log-normalization. Variable genes were identified using the standard deviation from the mean (using only non-zero values). Data were scaled and centered by regressing on library size and mitochondrial mRNA counts. Principle component analysis (PCA) was performed using variable genes. For TSNE analysis, clusters were identified using shared nearest neighbor (SNN) and reduction was performed based on PCA using the first 20 principle components. Marker genes defining each cluster were identified using Seurat's FindAllMarkers function, which employs a Wilcoxon rank sum test to determine significant genes. These marker genes were used to assign cluster identity to individual cell types. In order to establish identity the top 200 genes were analyzed on established gene expression data for immune cells which can be obtained at http://rstats.immgen.org/DataPage/ (Heng et al., 2008). In addition, cell clusters and markers were analyzed using the CellMarker database(Zhang et al., 2019): http://bio-bigdata.hrbmu.edu.cn/CellMarker/index.jsp, published signatures(Bindea et al., 2013; Liberzon et al., 2011; Newman et al., 2015), and existing literature (King, 2009; O'Garra, 1998; Vogelzang et al., 2008).

The single cell RNaseq data are available at the GEO: GSE136206.

5′ TCR/BCR Sequencing and Repertoire Analysis

Whole tumor mRNA coming from T11-apobec and KPB25Luv models treated for 7 days with ICI therapy was used as input for sequencing using each SMARTer Mouse TCR a/b Profiling Kit and SMARTer Mouse BCR IgG H/K/L Profiling Kit. First strand DNA-synthesis, amplification, and library generation followed protocol listed in the user manual. Following library selection additional cleanup utilized pippin prep and selection of fragments 400-900 bp. Paired-end, (2 × 300 bp) libraries were sequenced on the Illumina miSEQ next generation sequencer. Following demultiplexing, the resulting fastq files were analyzed using MIXCR(Bolotin et al., 2015), version 2.1.9-6. Top chain specific clone counts were extracted from resulting clones files and designated as those most expressed/highest numbers of counts detected. MIXCR determined clonotypes and their relative abundance were used to calculate shannon entropy(Bischof and Ibrahim, 2016; Magurran, 2013; Selitsky et al., 2019), a diversity index where lower entropy scores relate to low diversity/clonal restriction. Shannon entropy was calculated using the R package vegan. Results were visualized using GraphPad Prism.

External Gene Expression Data Analysis

Microarray data from Neoadjuvant chemotherapy treated breast tumors was downloaded from GEO: GSE32646(Miyake et al., 2012), Her2+ samples were excluded. Microarray data for the ISPY data was downloaded from the UNC microarray database and is also available from GEO: GSE22226 (Esserman et al., 2012). Samples were limited to those in the A/C/T arm, normal-like samples were removed. Data was median centered and column standardized prior to signatures analysis. Gene expression RNA-Seq data from the clinical trial CALG40601 was downloaded from GEO: GSE116335(Tanioka et al., 2018). Samples from the trastuzumab arm only were analyzed. The RNA-seq data from the melanoma clinical trial of ipilimumab was downloaded from DbGAP: phs000452.v2.p1(Van Allen et al., 2015). RNA-seq data for NCT01560663 is published (Echavarria et al., 2018). Fastq files were aligned to hg38.d1 genomes using STAR(Dobin et al., 2013). Resulting BAM files were sorted and indexed using Samtools and quality control was performed using Picard. Transcript read counts were determined was performed using Salmon(Patro et al., 2015; Patro et al., 2017). For RNA-Seq datasets, genes with no reads across any of the samples were removed. Salmon gene-level counts upper quartile normalized. Genes with an average expression less than 10 were filtered from the dataset. Genes were log2 transformed in Cluster 3.0(de Hoon et al., 2004) and zeros were preserved for signature analysis. Data was the median centered and column standardized. CALGB40601 data was limited to pretreatment samples from the Trastuzumab arms only. PAM50 subtypes were used from the publication(Tanioka et al., 2018). RNA-seq data for sorted immune cell types were queried using the online tool http://rstats.immgen.org/

MyGeneSet_New/index.html(Heng et al., 2008). Heatmaps were generated using the online tool and by selection of the depicted immune cell populations.

For the single-cell RNA-seq melanoma dataset (GEO: GSE120575(Sade-Feldman et al., 2018)), levels of genes were quantified as Transcripts Per Million (TPM). For each cell, the gene expression measurement was normalized by its total expression, multiplied by a scale-factor 10,000, and log-transformed. The collapsed gene signature score down to each sample was computed as follows: first, we took a sum of the normalized TPM values for each gene in the signature over all the cells in a given sample, then we calculated the median gene expression signature score for each sample.

Whole Exome Sequencing

For whole exome sequencing of mouse tumor, genomic DNA was isolated using a QIAGEN DNeasy blood and tissue kit (cat: 69506). As controls, we isolated DNA from whole-mouse mammary glands from Balbc and FVB mice. Libraries were constructed using the Agilent Sure Select XT kit with 1 ug of genomic DNA according to the manufacturer's protocol. DNA libraries were selected and amplified using the Agilent SureSelect Mouse All Exon kit. Final library size selection used approximately 300 bp fragments. Quality of libraries and captured exomes were measured using the Agilent Tapestation DNA 1000 and High Sensitivity D1000. Paired end (2 x100 bp) sequencing was done using Illumina HiSeq 2000/2500 sequencer at the UNC High Throughput Sequencing Facility. Sequences from fastq files were aligned to the mm10 using BWA mem(Li, 2013). Biobambam was used to process BAM files(Tischler and Leonard, 2014) and Picard was used for quality assessment. Strelka was used to call mutations and generate VCF files(Saunders et al., 2012). Variant filtering used mouse mammary gland sequencing from the appropriate genetic background. Somatic mutations were considered provided the variants were not detected in unexpected regions (ie- introns), or had evidence for being ''germline'' (shared in models of a known common background). In addition, subjective filtering was performed using IGV (for example, low-level detection of potential variant in the normal control). Neoantigen predictions were done using pvac-seq and followed published guidelines(Hundal et al., 2016). All raw DNA sequence fastq files have been deposited into the SRA: PRJNA506275.

DATA AND CODE AVAILABILITY

The published article includes all datasets and code generated in this study. The datasets generated during this study are available at GEO Datasets: GSE124821, GSE136206 and the Sequence Read Archive: PRJNA506275. Please see the key resources table or contact by contacting Charles M Perou (cperou@med.unc.edu) for further information.

Supplemental Figures

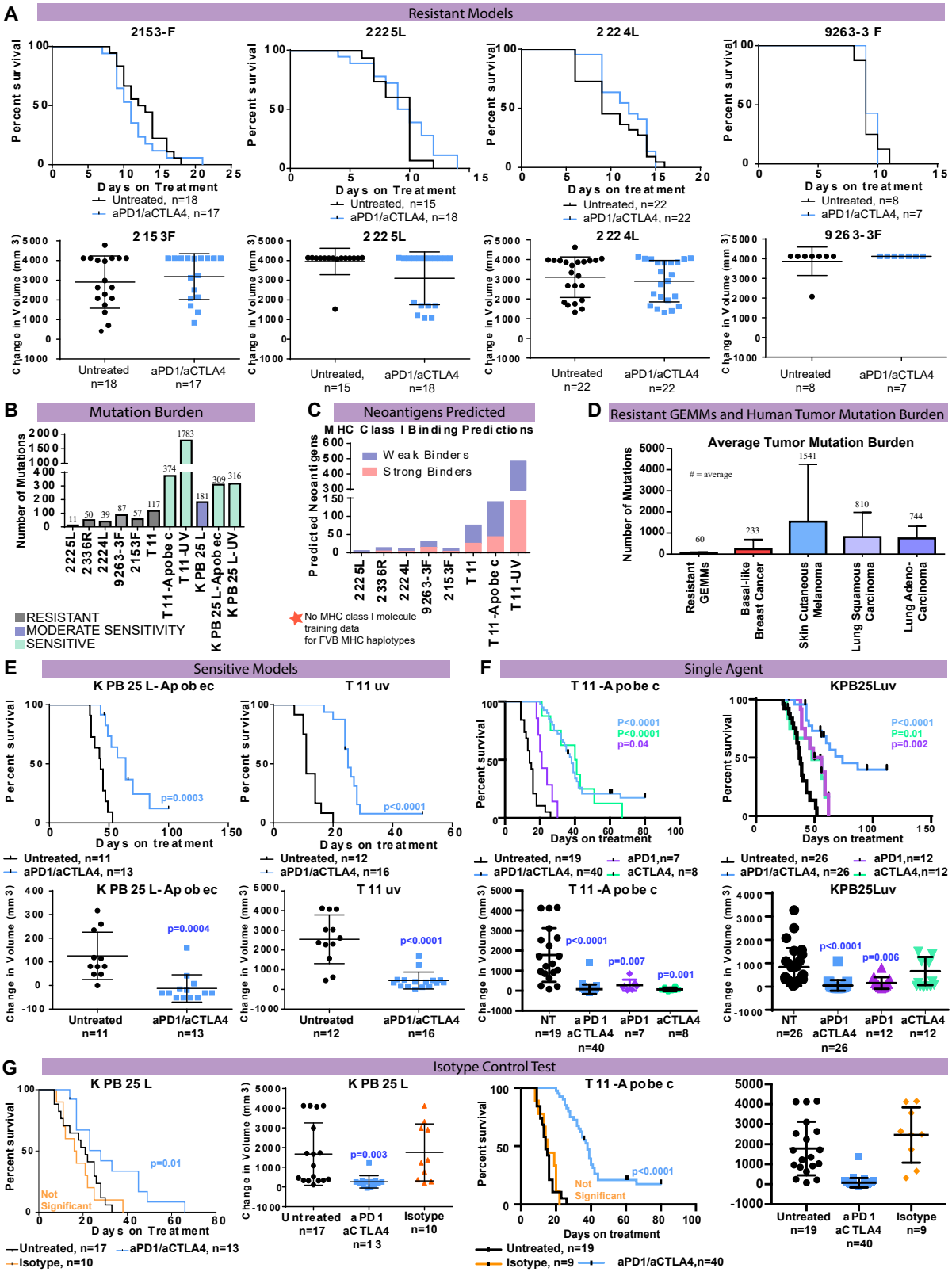

(legend on next page)

Figure S1. Somatic Mutation Burden and Response to Immune Checkpoint Therapy in Mouse Models of Triple-Negative Breast Cancer, Related to Figure 2

(A) Top, overall survival of non-treated tumors and treated tumors on anti-PD1/anti-CTLA4 therapy and lower panel showing 10-day acute response to anti-PD1/anti-CTLA4 therapy demonstrated models that are resistant to immune checkpoint therapy. (B) Somatic mutation burden as called by strelka in our mouse model cohort, with samples being color coded for response as depicted. (C) Neoantigen burden as predicted by pVac-Seq; strong binders were determined by best predicted binding threshold <500 mM and weak binders by predicted <2500 mM binding threshold. (D) Tumor mutation burden in resistant tumors and human cancers from the depicted TCGA study cohorts. (E) Top, overall survival of non-treated and treated tumors on anti-PD1/anti-CTLA4 therapy and lower, 10-day acute response to anti-PD1/anti-CTLA4 therapy demonstrated KPB25L-Apobec and T11-UV as models that are sensitive to immune checkpoint therapy. (F) Single-agent testing of anti-Pd1 or anti-Ctla4 in comparison to anti-PD1/anti-CTLA4 combination therapy, with overall survival on top and 10-day acute response showed on the lower. (G) Testing isotype control antibodies in the KPB25L and T11-Apobec models for anti-Pd1 and anti-Ctla4 shows no impact on top, overall survival, and lower, acute response. In Kaplan-Meier plots, p value mark results of Log-rank (Mantel-Cox) test. In box and whiskers dot plots, the bar signify the average and standard deviation from average. The p values represent two-tailed p value from standard unmatched t tests.

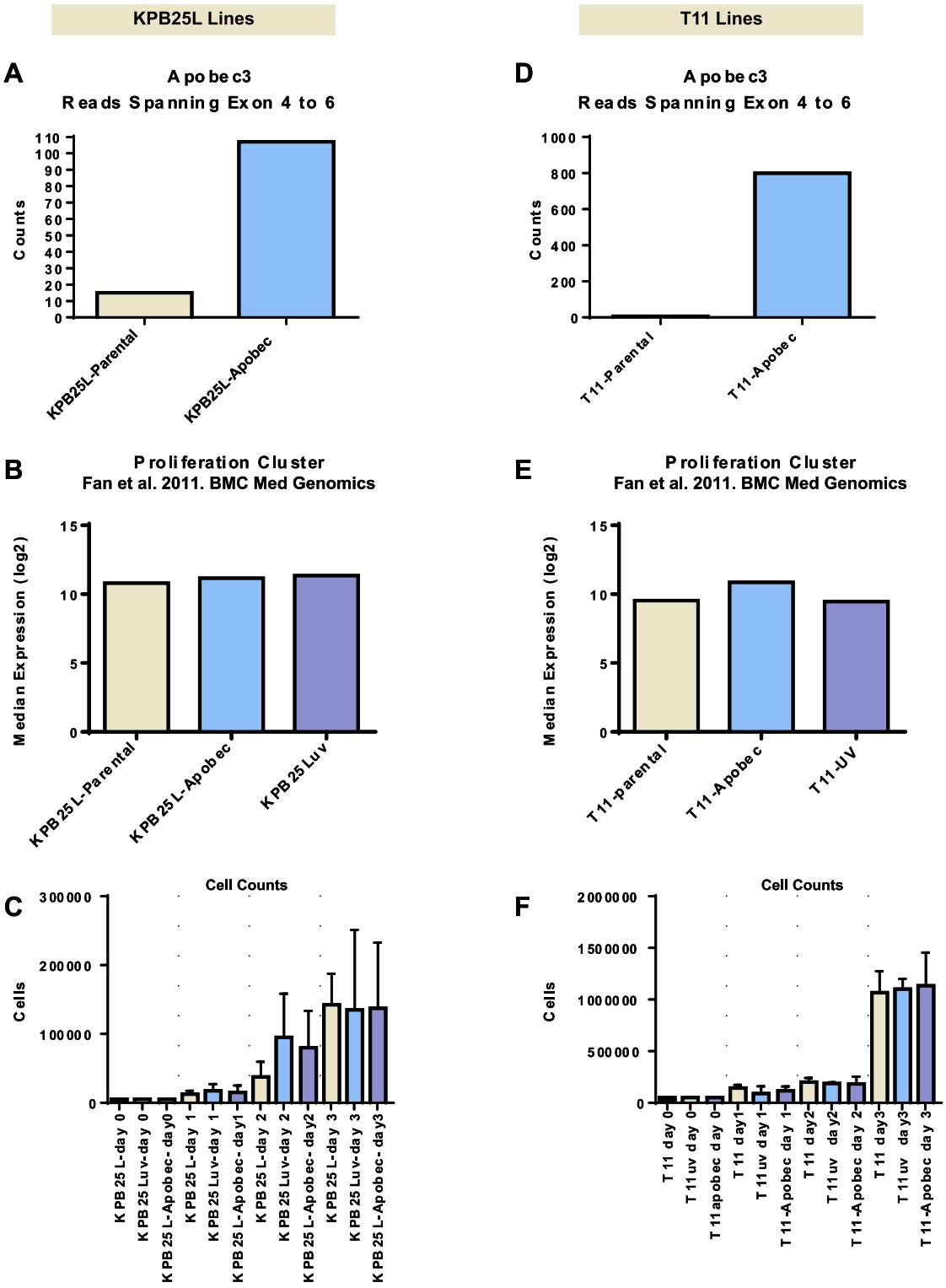

Figure S2. *In Vitro* Characterization of Mouse Tumor-Derived Cell Lines Mutagenized by Apobec3 or by Exposure to Short-Wave Ultraviolet Radiation, Related to Figure 2

(A) Apobec3 isoform2 overexpression in KPB25L-Apobec as compared to KPB25L parent (note the counts that isoform appropriately span/overlap exons 4 and 6 were identified using IGV sashimi plots and reported here). (B) Testing a proliferation signature (Fan et al., 2011) for median expression in Log2 normalized, uncentered, gene expression demonstrates no difference in proliferation features in KPB25L, KPB25L-Apobec, and KPB25Luv gene expression. (C) Cell counting

(legend continued on next page)

experiment to measure proliferation *in vitro* to compare KPB25L parent, KPB25Luv (UV mutagenized), and KPB25L-Apobec. (D) Apobec3 isoform2 overexpression as compared to T11 parent (note the counts that isoform appropriately span/overlap exons 4 and 6 were identified using IGV sashimi plots and reported here). (E) Testing a proliferation signature (Fan et al., 2011) for median expression in Log2 normalized, uncentered, gene expression demonstrates no difference in proliferation features in T11 parent, T11-Apobec, and T11-uv gene expression. (F) Cell counting experiment to measure proliferation *in vitro* to compare T11 parent, T11-uv (UV mutagenized), and T11-Apobec. Cell counting experiments were done in experimental triplicate.

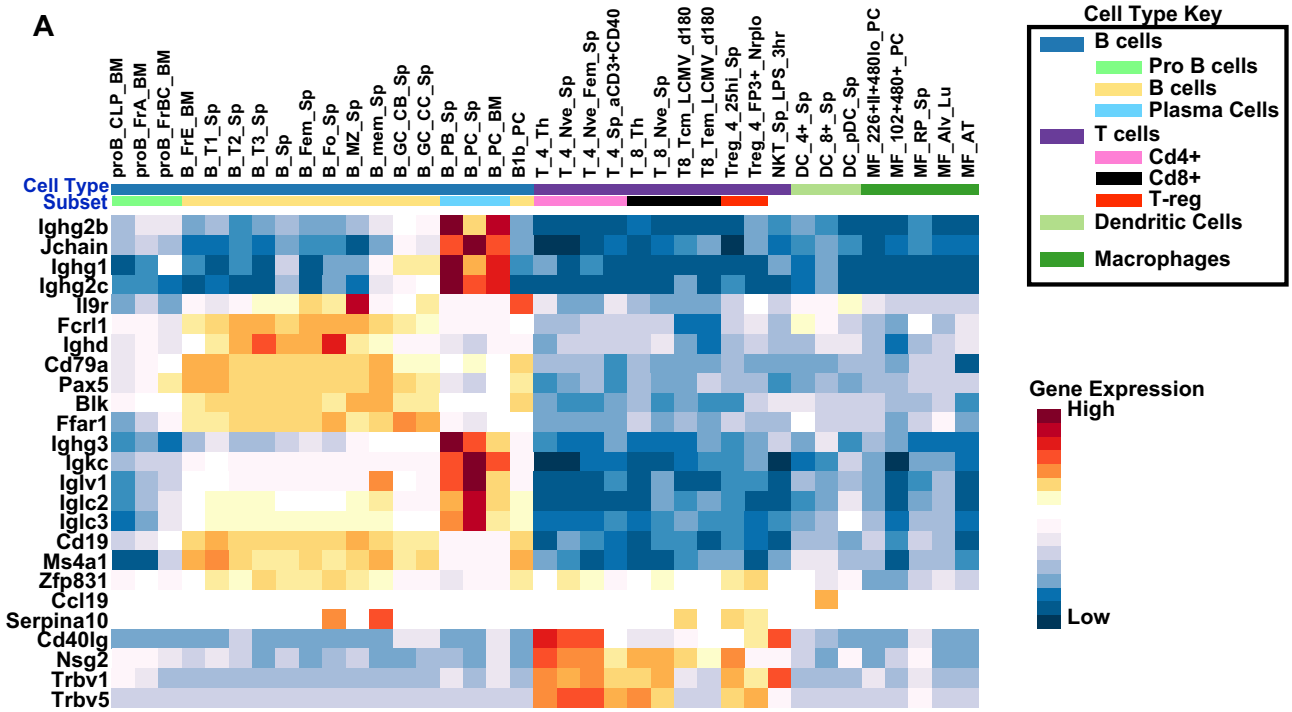

Immune Activity Signature Predictions

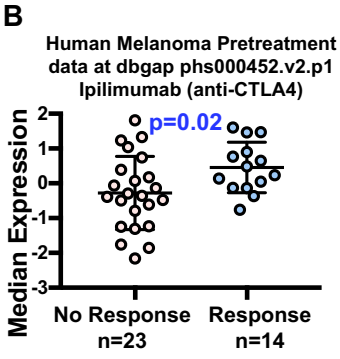

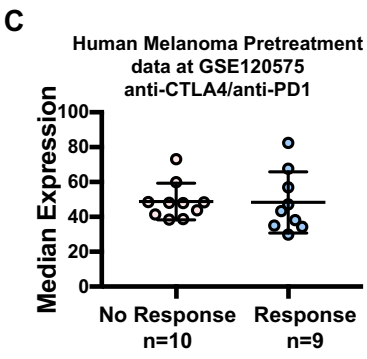

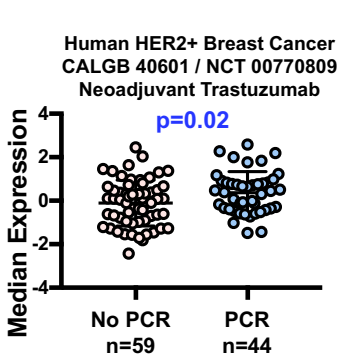

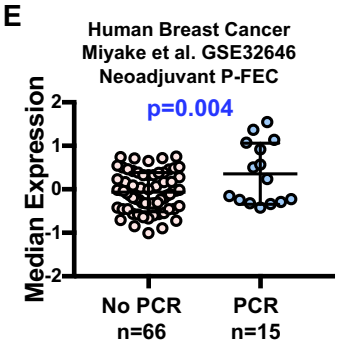

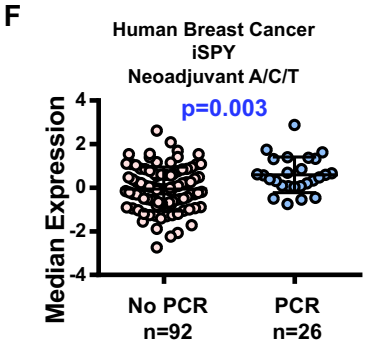

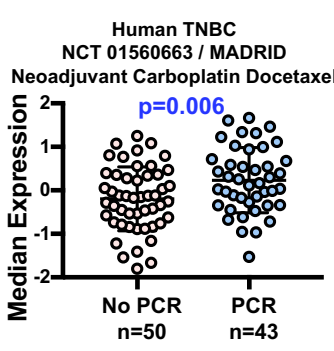

(legend on next page)

Figure S3. Supervised Analysis Comparing aPD1/aCTLA4 Therapy-Sensitive to aPD1/aCTLA4 Therapy-Resistant Mouse Mammary Tumors, Related to Figure 3

(A) An expression heatmap showing values of B cell/T cell co-cluster signature genes across RNA-seq data of sorted immune cells. Across the top, sample names as described on http://rstats.immgen.org/MyGeneSet_New/index.html. Below this, the color bar depicts the position of major immune cell types, as keyed on the right hand side. Immediately below, B cell and T cell subsets are depicted as color-coded. The heatmap depicts high expression to low expression as illustrated by the color bar. Heatmaps, clustering, and results generated using http://rstats.immgen.org/MyGeneSet_New/index.html. (B) Boxplot for expression of the immune activity cluster in pretreatment samples from a human melanoma study of anti-CTLA4 therapy (Van Allen et al., 2015). (C) Boxplot for the immune activity cluster in pretreatment samples from a human melanoma study of anti-PD1/ anti-CTLA4 therapy (Sade-Feldman et al., 2018). (D) Boxplot for expression of the immune activity cluster in pretreatment breast cancer samples from CALGB40601, trastuzumab arm (Tanioka et al., 2018). (E) Boxplot for expression of the immune activity cluster in pretreatment samples from the human breast cancer dataset GSE32646, excluding Her2+ samples; P-FEC = neoadjuvant paclitaxel followed by 5-fluorouracil/epirubicin/cyclophosphamide (Miyake et al., 2012). (F) Boxplot for expression of the immune activity cluster in pretreatment samples from the human breast cancer iSPY clinical trial; A/C/T arm = Doxorubicin hydrochloride (Adriamycin) and cyclophosphamide, followed by treatment with paclitaxel (Esserman et al., 2012). (G) Boxplot for expression of the immune activity cluster in pretreatment samples from the TNBC NCT 01560663 clinical trial (Echavarria et al., 2018). In boxplots, bars represent the average and standard deviation. The p values represent two-tailed p value from standard unmatched t tests; exception in (C) where Mann-Whitney tests where used due to non-Gaussian distribution. All tumors collected after 7days of treatment or non-treatment.

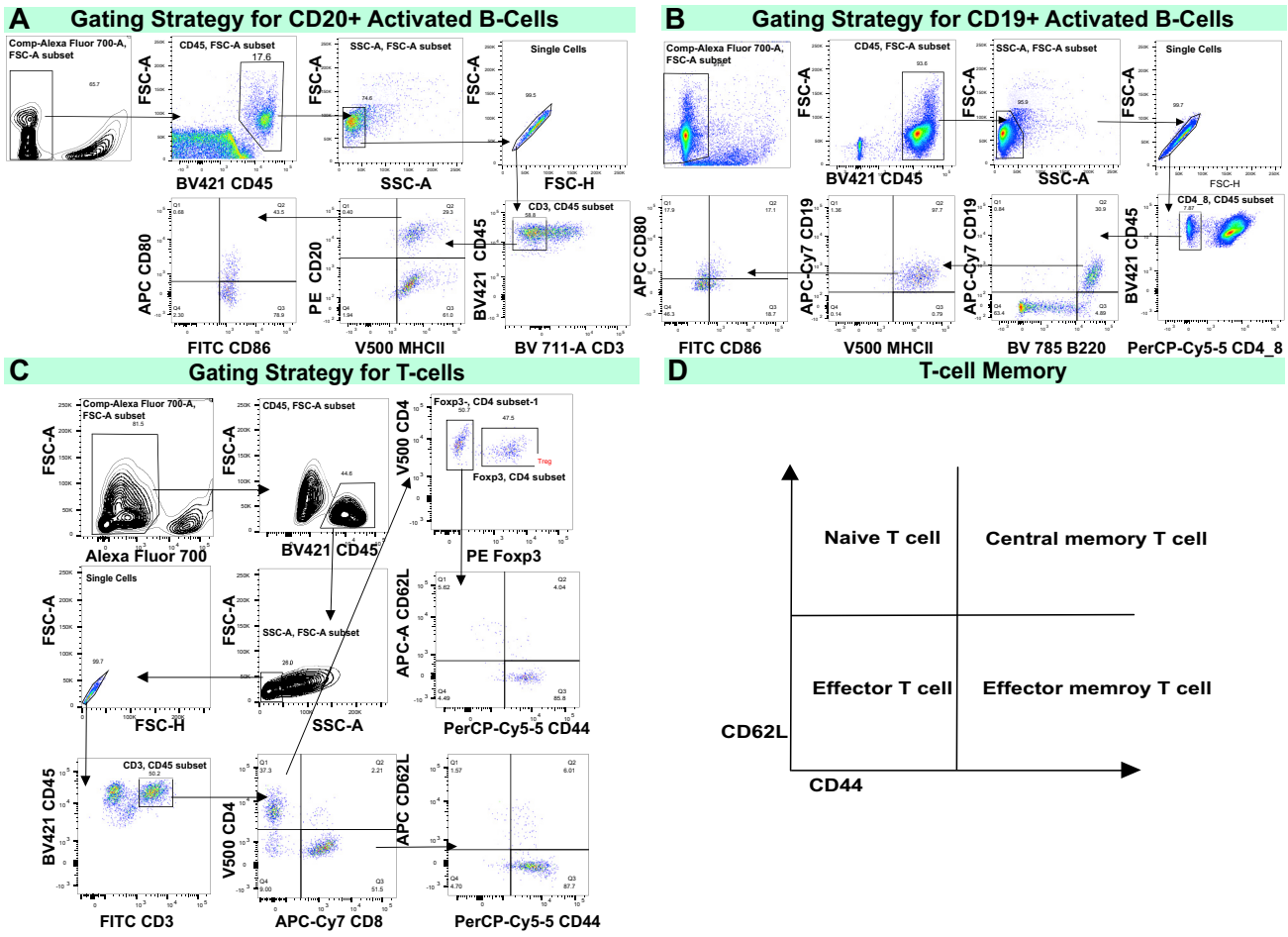

Figure S4. Flow Cytometry Gating Strategy, Related to STAR Methods

(A) Gating strategy for CD20+ Activated B cells as shown in the T11-Apobec model. (B) Gating strategy for CD19+ Activated B cells as shown in the KPB25Luv model. (C) Gating strategy for T cells (CD4+ or CD8+) to examine memory markers. (D) Key for to interpret memory markers profiles in T cells.

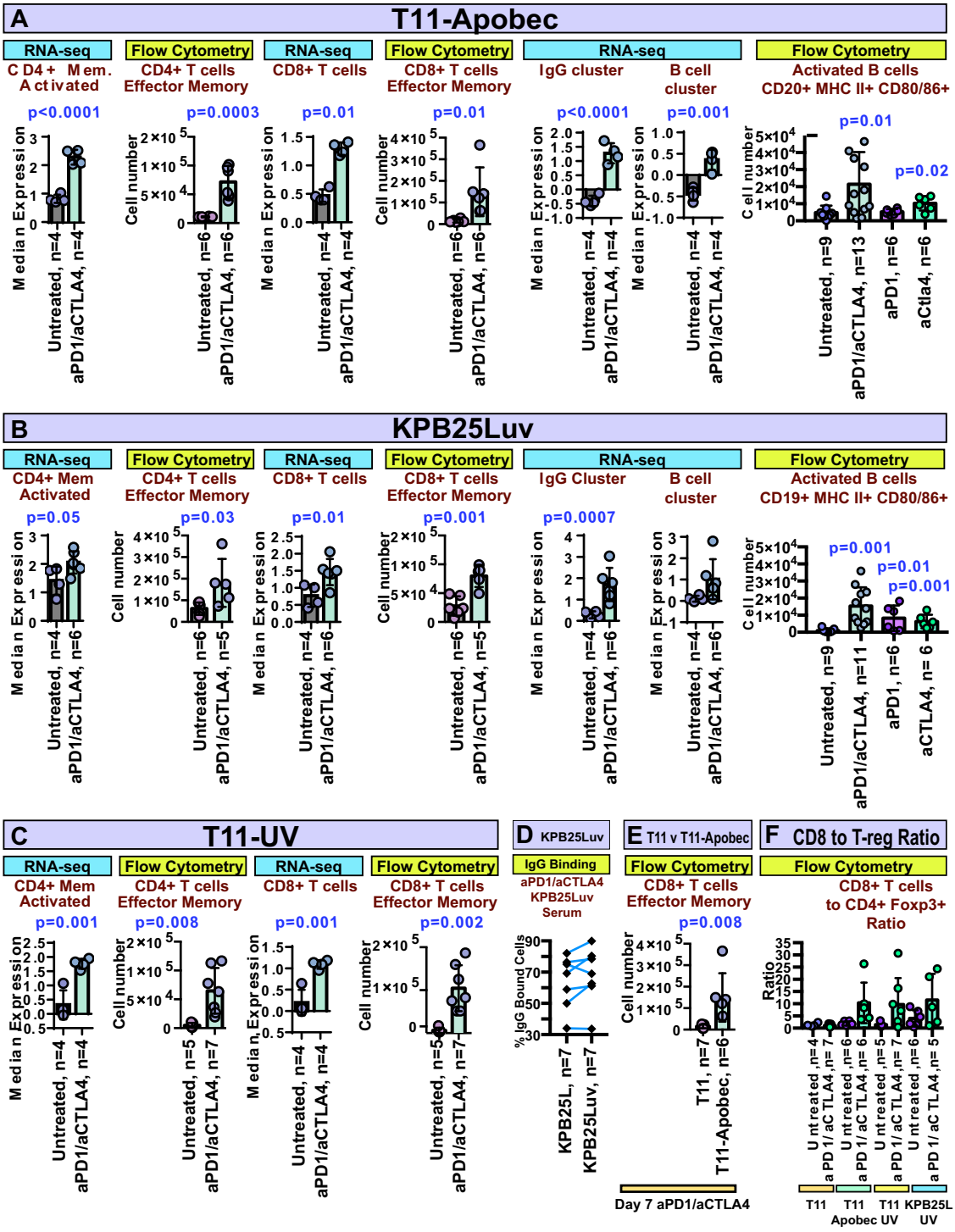

Figure S5. Validation of Immune Cell Signatures and Demonstration of Key Immune Features for Individual Tumor Cell Lines, Related to Figure 4

(A) Gene expression signatures and flow cytometry features for T cells and B cells in tumors of the T11-Apobec tumor bearing mice without or with anti-PD1/anti-CTLA4 (or single-agent) therapy. (B) Gene expression signatures and flow cytometry features for T cells and B cells in tumors of mice bearing KPB25Luv tumor model without or with anti-PD1/anti-CTLA4 (or single-agent) therapy. (C) Gene expression signatures and flow cytometry features for T cells in mice bearing the T11-uv tumor model without or with anti-PD1/anti-CTLA4 therapy. (D) IgG binding assay using serum from ICI treated KPB25Luv bearing mice. Lines depict matched sera testing on parent and mutagenized cells. (E) Flow cytometry comparing the number of CD8+ T cells with effector memory status in tumors of mice

(legend continued on next page)

receiving the parent T11 line or T11-Apobec without or with anti-PD1/anti-CTLA4 therapy. (F) A comparison of the CD8+ T cells as a ratio to CD4+ Foxp3+ T cells in individual tumor lines without or with anti-PD1/anti-CTLA4 therapy. All panels depict tumors isolated following 7 days past the therapeutic start point of a 5mm diameter tumor. In bar plots, the bar represents the average and standard deviation from average. The p values represent two-tailed p value from standard unmatched t tests.

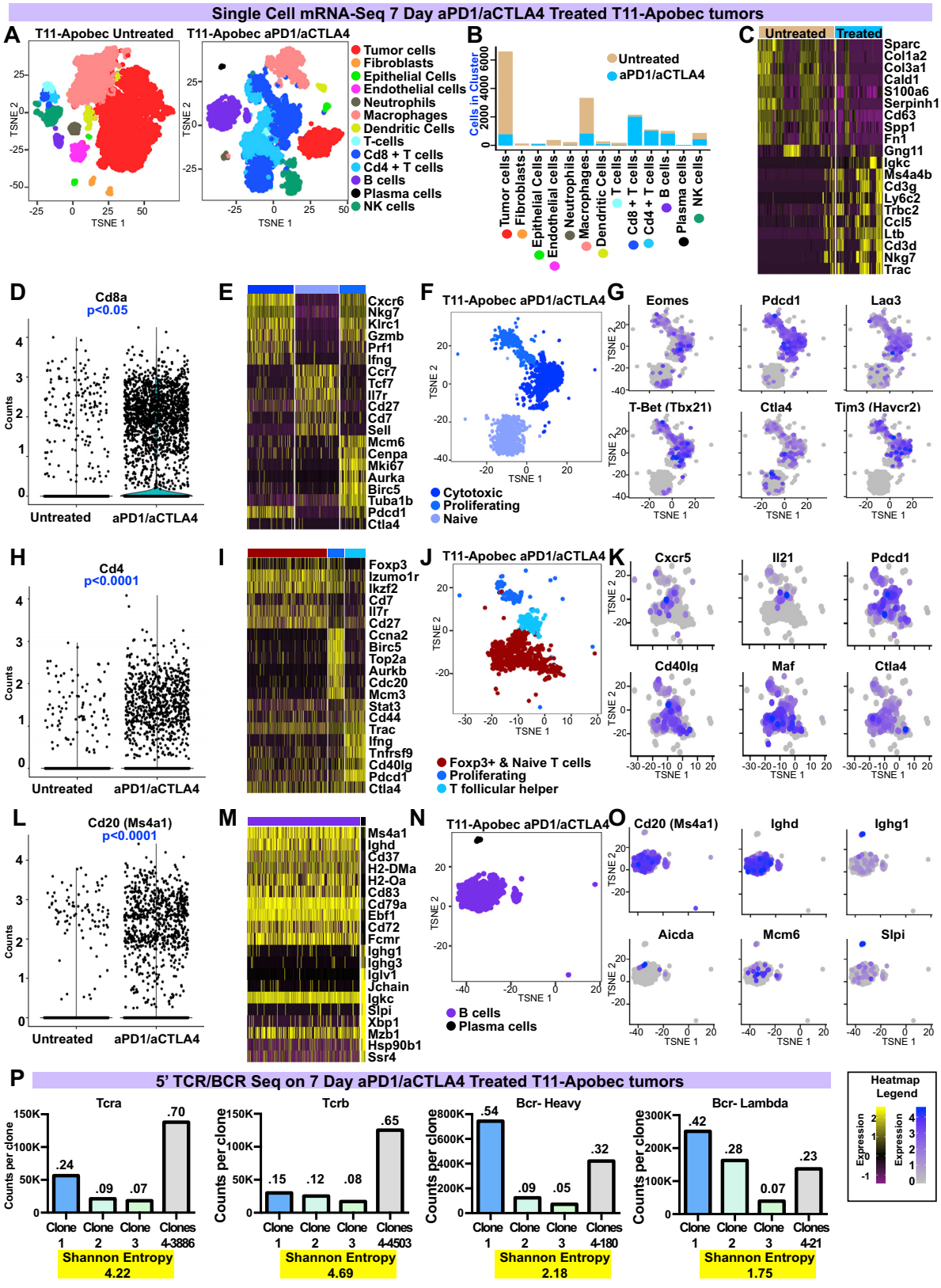

(legend on next page)

Figure S6. Single-Cell RNA-Seq of T11-Apobec Tumors with or without Anti-PD1/Anti-CTLA4 Therapy, Related to Figure 5

(A) TSNE analysis of all cells that passed quality control in untreated and aPD1/aCTLA4 treated T11-Apobec tumors. Cells are color coded according to dominant cell type (identified by gene expression profiles) found in each cluster. (B) The numerical distribution of cell types between treated and non-treated tumor cells. (C) Heatmap depicting supervised analysis comparing treated and non-treated tumor cells. (D) Violin plot of Cd8a mRNA levels in cells of treated and non-treated tumor cells. (E) Heatmap for results of Seurat marker analysis of significant genes between clusters of CD8+ T cells (as identified in A), shown are significant genes along with checkpoint Pdcd1 and Ctla4 mRNA (n = 20). (F) Classification of CD8+ T cell clusters based on gene expression profiles. Note the color coding is also mapped above the heatmap in E. (G) Feature plot showing expression of key markers across CD8+ T cell clusters. (H) Violin plot depicting Cd4 mRNA levels in cells of treated and non-treated tumor cells. (I) Heatmap depicting results of Seurat marker analysis of significant genes between clusters of CD4+ T cells (as identified in A), shown are significant genes along with checkpoint Pdcd1 and Ctla4 mRNA (n = 20). (J) Classification of CD8+ T cell clusters based on gene expression profiles. Color coding is also mapped to the heatmap in I. (K) Feature plot showing expression of key markers across CD4+ T cell clusters. (L) Violin plot of Cd20 mRNA levels in cells of treated and non-treated tumor cells. (M) Heatmap for results of Seurat marker analysis of significant genes between clusters of B cells (as identified in A; n = 20). (N) Classification of B cell clusters based on gene expression profiles. Color coding is also mapped to the heatmap in M. (O) Feature plot showing expression of key markers across B cell clusters. (P) Results of 5′ TCR/BCR sequencing. For each boxplot the number counts detected for each clone, as identified by MIXCR, is shown along with the calculated Shannon entropy (where higher values indicate high diversity/low clonality). Above each bar, indicates the percent of all reads occupied by a clone(s). Note the fourth bar groups all clones not represented by the top 3 clones. All heatmap values can be found according the legend. All violin plots depict the mean and SEM. Markers were identified using Seurat and Wilcoxon rank sum testing.

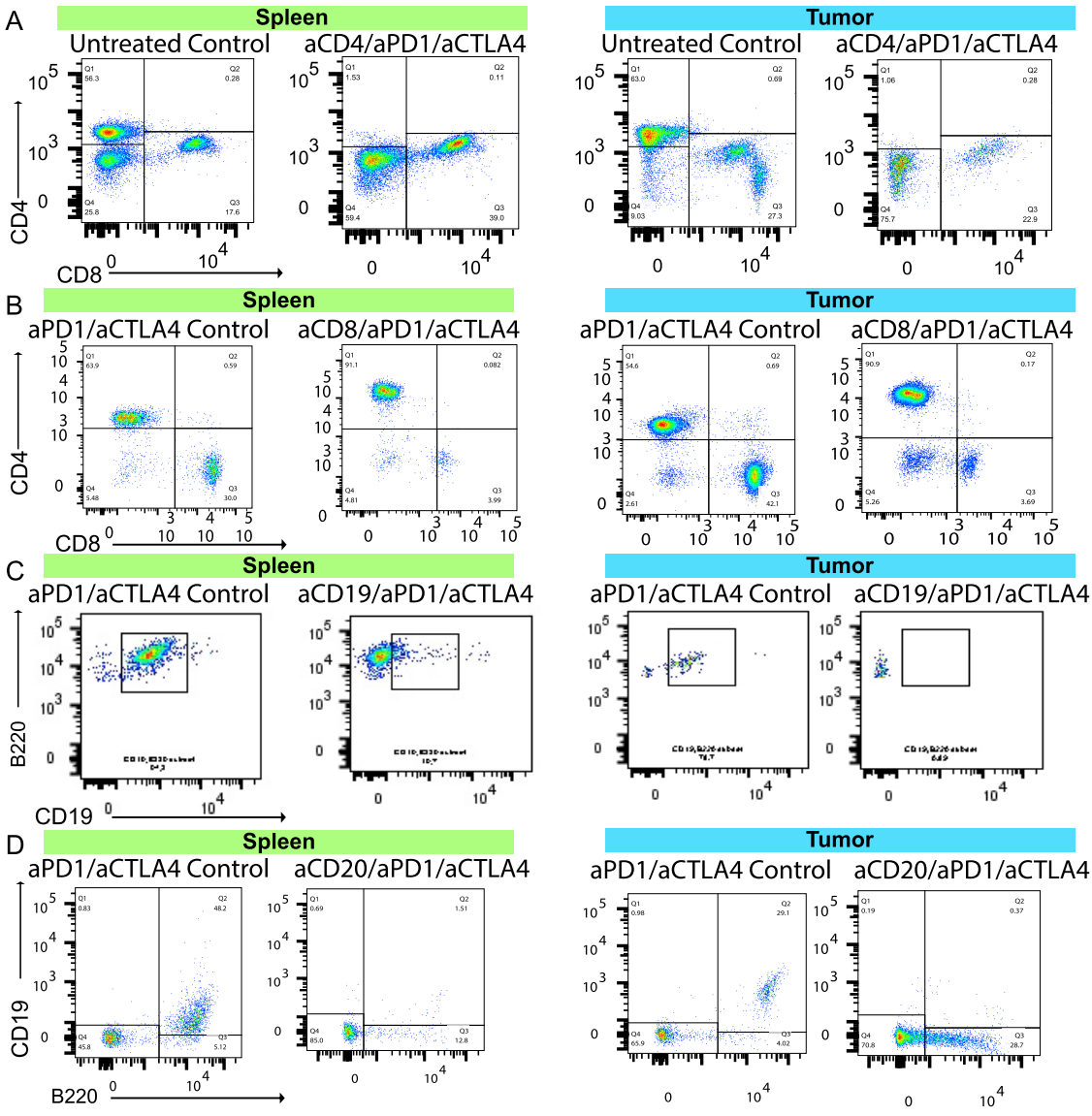

Figure S7. Flow Cytometry Analysis of Targeted Immune Cell Depletion in Tumors and Spleens in Tumor-Bearing Mice Receiving Anti-PD1/Anti-CTLA4 Therapy, Related to Figure 6

(A) Flow cytometry plots of CD4+ T cell depletion at tumor and spleen in tumor bearing mice receiving anti-PD1/anti-CTLA4 therapy. (B) Flow cytometry plots of CD8+ T cell depletion at tumor and spleen in tumor bearing mice receiving anti-PD1/anti-CTLA4 therapy. (C) Flow cytometry plots of CD19 inhibition at tumor and spleen in tumor bearing mice receiving anti-PD1/anti-CTLA4 therapy. (D) Flow cytometry plots of CD20+ B cell depletion at tumor and spleen in tumor bearing mice receiving anti-PD1/anti-CTLA4 therapy.

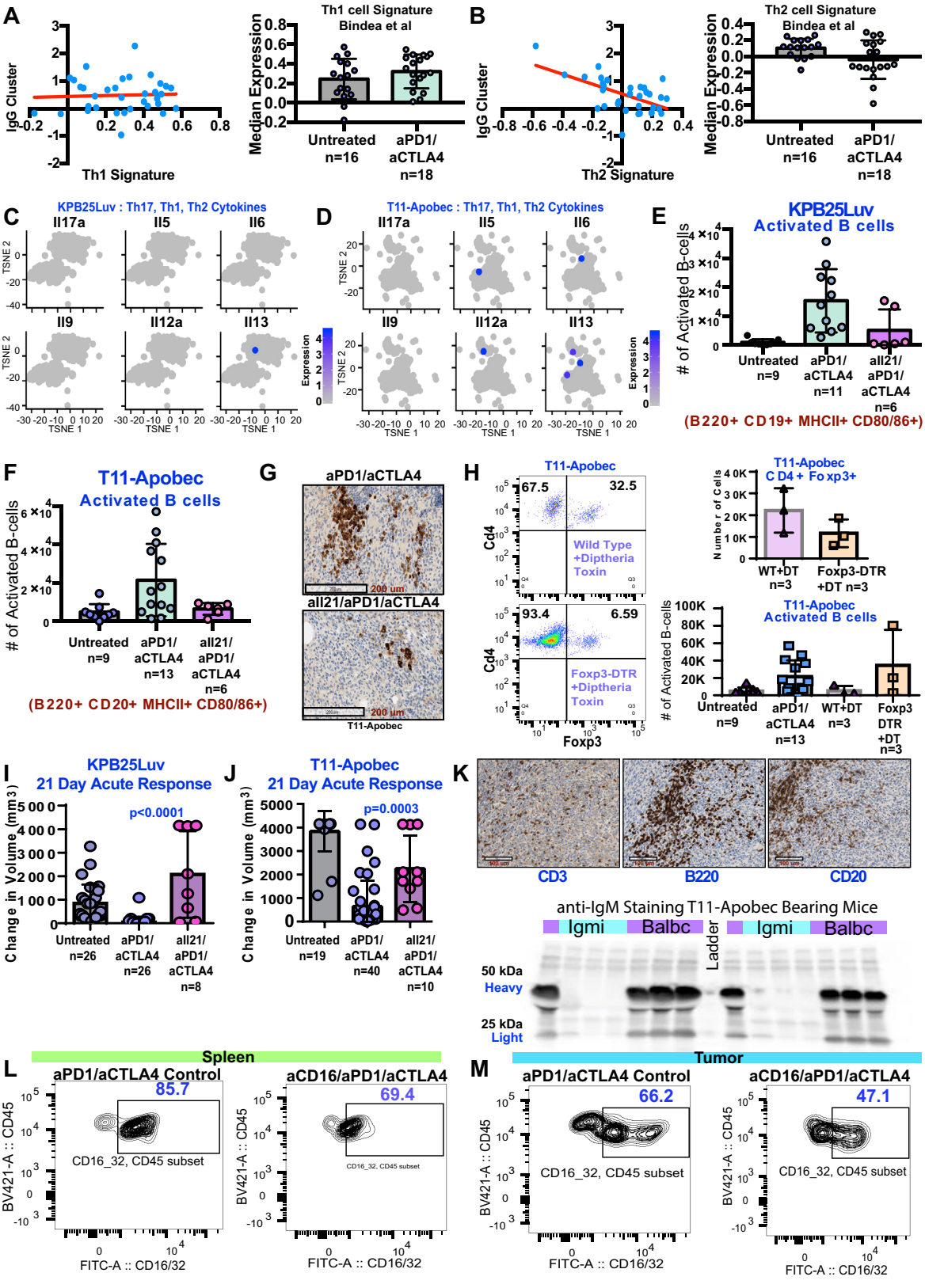

(legend on next page)

Figure S8. Testing B Cell Activation and IgG Functionality during Immune Checkpoint Therapy, Related to Figure 7

(A) Left: X-Y plot depicting relationship between a IgG signature and Th1 T cell signature in sensitive tumors (mRNA-seq) at day 7 with or without therapy. Right: Boxplot of expression of a T helper 1 signature in sensitive tumors (mRNA-seq) at day 7 with or without therapy. (B) Left: X-Y plot depicting relationship between the IgG signature and a T helper 2 cells in sensitive tumors (mRNA-seq) at day 7 with or without therapy. Right: Boxplot of expression of a T helper 2 signature in sensitive tumors (mRNA-seq) at day 7 with or without therapy. (C) Feature plot of T helper 17, 1, or 2 cytokines in KPB25Luv tumor CD4+ T cell clusters. (D) Feature plot of T helper 17, 1, or 2 cytokines in T11-Apobec tumor CD4+ T cell clusters. (E) Quantification of flow cytometry for activated B cells (B220+, Cd19+, MHC II +, Cd80+ or Cd86+) in KPB25Luv tumors given aPD1/aCTLA4 therapy with or without IL21 blockade. (F) Quantification of flow cytometry for activated B cells (B220+, Cd20+, MHC II +, Cd80+ or Cd86+) in T11-Apobec tumors given aPD1/aCTLA4 therapy with or without IL21 blockade. (G) IHC staining for IgG-kappa chain in untreated,aPD1/aCTLA4 treated, or IL21blocked aPD1/CTLA4 treated T11-Apobec tumors. (H) Left: Flow cytometry plot demonstrating diphtheria toxin depletion of Foxp3+ cells exclusively in T11-Apobec tumors implanted into the Foxp3-DTR GEMM. Right top: Quantification of T_{regs} in WT and Foxp3-DTR GEMMs (bearing T11-Apobec) given diphtheria toxin. Right bottom: flow cytometry quantification of activated B cells in Foxp3-DTR GEMMs given diphtheria toxin (DT) to deplete T_{regs}. (I) 21 day acute response for KPB25Luv bearing mice given ICI or ICI with IL21 blockade. (J) 21 day acute response for T11-Apobec bearing mice given ICI or ICI with IL21 blockade. (K) Top: IHC for CD3, B220, or CD20 on day 7 T11-Apobec tumors implanted into Igmi mice demonstrates these mice to be intact for B cells and T cells. Bottom: western blot analysis of serum IgM for Igmi mice (blue bars) or Balbc mice (purple bars) bearing T11-Apobec tumors. (L) Flow cytometry results for anti-CD16/32-FITC binding to splenocytes in mice either treated with anti-PD1/anti-CTLA4 combination therapy or anti-CD16/32 (shortened as anti-CD16) with anti-PD1/anti-CTLA4. (M) Flow cytometry results for anti-CD16/32-FITC binding to cells in tumors of mice either treated with anti-PD1/anti-CTLA4 combination therapy or anti-CD16/32 (shortened as anti-CD16) with anti-PD1/anti-CTLA4. In X-Y plots, p values were determined by linear regression analysis. In box and whiskers dot plots, the bar represents the average and standard deviation from average.